

# A *Chandra*/ACIS Study of 30 Doradus I. Superbubbles and Supernova Remnants

Leisa K. Townsley<sup>1</sup>, Patrick S. Broos<sup>1</sup>, Eric D. Feigelson<sup>1</sup>, Bernhard R. Brandl<sup>2</sup>, You-Hua Chu<sup>3</sup>, Gordon P. Garmire<sup>1</sup>, George G. Pavlov<sup>1</sup>

## ABSTRACT

We present an X-ray tour of diffuse emission in the 30 Doradus star-forming complex in the Large Magellanic Cloud using high-spatial-resolution X-ray images and spatially-resolved spectra obtained with the Advanced CCD Imaging Spectrometer aboard the *Chandra X-ray Observatory*. The dominant X-ray feature of the 30 Doradus nebula is the intricate network of diffuse emission generated by interacting stellar winds and supernovae working together to create vast superbubbles filled with hot plasma. We construct maps of the region showing variations in plasma temperature ( $T = 3\text{--}9$  million degrees), absorption ( $N_H = 1\text{--}6 \times 10^{21} \text{ cm}^{-2}$ ), and absorption-corrected X-ray surface brightness ( $S_X = 3\text{--}126 \times 10^{31} \text{ ergs s}^{-1} \text{ pc}^{-2}$ ). Enhanced images reveal the pulsar wind nebula in the composite supernova remnant N157B and the *Chandra* data show spectral evolution from non-thermal synchrotron emission in the N157B core to a thermal plasma in its outer regions. In a companion paper we show that R136, the central massive star cluster, is resolved at the arcsecond level into almost 100 X-ray sources. Through X-ray studies of 30 Doradus the complete life cycle of such a massive stellar cluster can be revealed.

*Subject headings:* HII regions — stars: winds, outflows — galaxies: star clusters — ISM: individual (30 Doradus) — supernova remnants — X-rays: ISM

## 1. INTRODUCTION

Images of spiral and irregular galaxies have been defined historically by regions of massive star formation, signposts demarcating important features such as spiral arms, bars, and starbursts. They remind us that galaxies really are evolving, with continuous injection of energy and processed material into the galaxy. Massive star-forming regions (MSFRs) present us with a microcosm of starburst astrophysics, where stellar winds from O and Wolf-Rayet (WR) stars compete with supernovae (SNe) to carve up the neutral medium from

which they formed, igniting a new generation of stars. With X-ray observations, we see the sources that shape the larger view of a galaxy, injecting energy and processed material into the disk and halo ISM through winds, ionization fronts, SNe, superbubbles, and chimneys. About 80% of all SNe occur in superbubbles, so cosmic rays generated by SNe also may be accelerated in superbubbles (e.g. Higdon et al. 1998; Parizot et al. 2004). X-ray observations probe different energetic components than traditional visual and infrared (IR) studies, penetrating the obscuring material of the natal cloud while minimizing confusion from foreground and background objects.

X-ray studies also detect the presence of past SNe through the shocks in their extended remnants. Some superbubbles are well-known bright X-ray sources, where multiple SNe from past OB stars produce soft X-rays filling bubbles 50–100 pc in size with  $L_x \sim 10^{35\text{--}36} \text{ ergs s}^{-1}$  (Chu & Mac

<sup>1</sup>Department of Astronomy & Astrophysics, 525 Davey Laboratory, Pennsylvania State University, University Park, PA 16802

<sup>2</sup>Sterrewacht Leiden, PO Box 9513, 2300 RA Leiden, The Netherlands

<sup>3</sup>Astronomy Department, University of Illinois at Urbana-Champaign, 1002 West Green Street, Urbana, IL 61801

Low 1990), while others (not recently brightened by such “cavity” SNe) are X-ray faint (Chu et al. 1995a). MSFRs thus exhibit a complicated mixture of point and extended structures that are easily confused by low-resolution X-ray telescopes. 30 Doradus (30 Dor) is a classic example of this. The *Chandra X-ray Observatory* (Figure 1 and Townsley et al. 2005b, hereafter Paper II) and *XMM-Newton* (Dennerl et al. 2001) share the highest-quality views yet achieved of this extraordinary and complicated X-ray field.

30 Dor is a field of superlatives. Located in the Large Magellanic Cloud (LMC), it is the most luminous Giant Extragalactic HII Region (GEHR) and “starburst cluster” in the Local Group. It hosts the massive compact star cluster R136 (Feast et al. 1960, called “RMC 136” in SIMBAD), a testbed for understanding recent and ongoing star formation in the 30 Dor complex (Walborn et al. 2002). Although R136, with a mass of  $\sim 6 \times 10^4 M_{\odot}$  (Brandl 2005), does not quite qualify as a “super star cluster” (Meurer et al. 1995), it has more than 50 times the ionizing radiation of the Orion Nebula. Nearby, one finds the large supernova remnant (SNR) N157B (30 Dor B), embedded in an HII region generated by the OB association LH 99 (Chu et al. 1992) and containing an X-ray pulsar (Marshall et al. 1998). *ROSAT* images showed two fainter sources associated with WR stars near the central star cluster, at least five plasma-filled superbubbles, and the N157B SNR (Wang 1995, 1999). 30 Dor’s proximity and complexity provide us with a unique and important microscope into the starburst phenomenon in galaxies.

Figure 1 illustrates the spatial and spectral complexity of the X-ray emission from 30 Dor with a smoothed image of our *Chandra* observation obtained with the Advanced CCD Imaging Spectrometer (ACIS). The aimpoint of the  $17' \times 17'$  ACIS Imaging Array (ACIS-I) was the R136 cluster. At  $D = 50$  kpc, the distance we assume throughout this paper and Paper II,  $1' \sim 14.5$  pc, so ACIS-I covers  $\sim 240$  pc  $\times$  240 pc. Two off-axis CCDs from the ACIS Spectroscopy Array (ACIS-S) were operated for this observation, adding a  $\sim 120$  pc  $\times$  240 pc image of nearby interesting structures (see Figure 2), albeit with poor spatial resolution. A more finely binned image of the ACIS-I data, highlighting the X-ray point sources

and showing a J2000 coordinate grid, can be found in Figure 1 of Paper II.

30 Dor lies at the confluence of two LMC supergiant shells and just the main nebula is  $\sim 250$  pc in diameter. Since the LMC is viewed nearly face-on, confusion between 30 Dor and other disk structures is minimized. SNe pervade the region but most go undetected due to age and environment (Chu & Mac Low 1990). Nearby are two pulsars (B0540–69.3 in the SNR N158A and J0537–6910 in the SNR N157B) and SN1987A (Figure 2). Wide-field ground-based H $\alpha$  images (e.g. Meaburn 1984; Chu & Mac Low 1990; Wang 1999), enhanced by recent *HST* (Walborn et al. 2002) and *Spitzer* data<sup>1</sup>, show that the combined actions of stellar winds and SNe from several generations of high-mass stars in 30 Dor have carved its ISM into an amazing display of arcs, shells, pillars, voids, and bubbles, ranging over spatial scales of 1–100 pc (Brandl 2005).

This field provides a unique bridge between Galactic giant HII regions (e.g. W49A, W51A, NGC 3603) and GEHRs (e.g. NGC 5471 and other regions in M101, Chen et al. 2005). 30 Dor is the result of multiple epochs of high-mass star formation in a vast molecular cloud complex chemically enriched by many SNe; it has no Galactic counterpart in terms of mass or complexity of its star formation history and is not even equalled by other GEHRs in the Local Group. It provides us with a unique view of the most fundamental building block of the starburst phenomenon in galaxies; currently we are not able to resolve comparable star-forming complexes in starburst galaxies, only those many times larger and more powerful (e.g. NGC 253, NGC 7714/7715; Strickland et al. 2002; B. Smith et al. 2005).

In §2 we provide a brief summary of X-ray observations of the 30 Dor complex. Our *Chandra* observations and data analysis are outlined in §3. An overview of the X-ray morphology and global spectral properties of the complex is presented in §4. The rest of the paper provides more in-depth studies of specific diffuse X-ray components of the 30 Dor complex: the superbubbles centered on R136 (§5), the SNR N157B (§6), and other diffuse structures, with a comparison to the H $\alpha$  kin-

---

<sup>1</sup><http://www.spitzer.caltech.edu/Media/releases/ssc2004-01/release.shtml>

matic study of 30 Dor by Chu & Kennicutt (1994) (§7). We conclude with a comparison of the X-ray data to recent H $\alpha$  and IR data and a summary of our results. The X-ray point source population of 30 Dor revealed by this dataset is described in Paper II.

## 2. PAST X-RAY OBSERVATIONS

### 2.1. The Large Magellanic Cloud and 30 Doradus

X-rays were first detected from the LMC in 1968 using rocket-launched proportional counters (Mark et al. 1969). An early survey of the LMC with the *Einstein Observatory* (Long et al. 1981) found 75 discrete sources associated with the galaxy, including 25 SNRs and about 25 other extended sources. A re-analysis of the *Einstein* LMC survey resulted in a point source catalog of 105 sources, “roughly half” associated with the LMC (Wang et al. 1991); the other sources are foreground stars or background active galactic nuclei (AGN). These authors noted source confusion associated with the 30 Dor complex.

Detailed studies of 30 Dor and other LMC superbubbles were performed with *Einstein* (e.g. Chu & Mac Low 1990; Wang & Helfand 1991a,b); they concluded that the bright, diffuse X-ray emission filling the 30 Dor superbubbles was probably created by off-center cavity SNe inside the superbubbles shocking the superbubble shells. Extending the work of Meaburn (1984), Chu & Kennicutt (1994) performed a detailed echelle study of the kinematics of 30 Dor and compared their findings to the *Einstein* data, concluding that 30 Dor is dominated by a hierarchy of expanding structures with spatial scales ranging over 1–100 pc and expansion velocities of 20–200 km s $^{-1}$ . The diffuse X-ray sources are coincident with these expanding shells, with the brightest X-ray emission coincident with high-velocity features. Chu & Kennicutt (1994) argued that both the high-velocity features and the X-ray emission are related to high-velocity shocks created by fast stellar winds and SNe.

Two catalogs of LMC point sources emerged from the *ROSAT Observatory*; a few sources (often SNRs or SNR candidates) are associated with the 30 Dor complex (Haberl & Pietsch 1999; Sasaki et al. 2000). In mosaicked *ROSAT* maps of the hot ISM in the LMC, 30 Dor is an outstanding

feature—hotter, brighter, and at higher pressure than most other parts of the galaxy (Snowden & Petre 1994; Points et al. 2001; Sasaki et al. 2002). *ROSAT* studies of individual LMC superbubbles showed that several are X-ray faint (Chu et al. 1995a), consistent with earlier conclusions that superbubbles are only brightened in X-rays when SNe hit the shell walls, while others exhibit “breakout regions” and may be venting hot gas into the LMC’s ISM (Dunne et al. 2001).

A *ROSAT/PSPC* study of 30 Dor reported 22 point sources within the 30 Dor nebula, including sources associated with R136 and N157B (Norci & Ögelman 1995). Spectral fits to the diffuse emission yielded  $N_H \sim 8 \times 10^{21} \text{ cm}^{-2}$  and  $kT \sim 0.4 \text{ keV}$ , with a luminosity (0.1–2.4 keV) of  $L_X = 3\text{--}6 \times 10^{37} \text{ ergs s}^{-1}$  depending on choice of background. Since the Galactic absorbing column toward 30 Dor is  $7 \times 10^{20} \text{ cm}^{-2}$ , most of the absorption found in their spectral fits is local to 30 Dor. They confirm the *Einstein* results (Wang & Helfand 1991a) that the diffuse X-ray emission fills the voids in the H $\alpha$  emission and further conclude that stars in 30 Dor contribute  $\leq 2\%$  of its total X-ray luminosity. While Norci and Ögelman note that the central cluster R136 is too young to have produced X-ray binaries that could contribute to the X-ray emission in the region, a *ROSAT/HRI* study suggested that the two point sources found by HRI were associated with the WR stars R140a2 (a WN6 binary) and Melnick 34 (WN4.5) and could be WR/black hole binaries (Wang 1995). This conjecture was supported by *ASCA* spectral results that indicated hard X-ray emission from the central regions of 30 Dor. Further *ROSAT/HRI* and *ASCA* observations led Wang (1999) to conclude that the diffuse emission came from 2–9 MK thermal plasmas and that the primary mechanism to explain the temperature and X-ray luminosity of this emission is mass-loading via mixing of the hot wind-generated gas with HII gas from the large number of ionization fronts in the region (Scowen et al. 1998).

The first light image from the *XMM-Newton Observatory* was obtained from a 106 ks pointing just west of the main 30 Dor nebula (Dennerl et al. 2001). This observation yielded broad-band (0.1–10 keV) spectra for several important objects in the neighborhood of 30 Dor: N157B, the Honeycomb Nebula (a SNR, Chu et al. 1995b), and

faint diffuse emission northwest of 30 Dor (Dennerl et al. 2001), as well as several likely AGN seen through the LMC disk (Haberl et al. 2001). A 38 ks *XMM* observation of N157B (Observation 0113020201, PI Aschenbach) images even more of the main 30 Dor nebula; although it is beyond the scope of this effort to include that observation in this paper, future efforts to obtain spectra of various features in 30 Dor from this dataset would be worthwhile.

## 2.2. N157B and PSR J0537–6910

The N157B SNR has itself been the subject of many X-ray studies. A known radio source, it was first detected in X-rays by *Einstein* (Long & Helfand 1979). A later *Einstein* study (Clark et al. 1982) demonstrated that its spectrum showed no strong emission lines and was non-thermal, well-fit by a power law with slope  $\Gamma = 2.9$ ,  $N_H = 1.2 \times 10^{21} \text{ cm}^{-2}$ , and luminosity (0.5–4.5 keV) of  $L_X = 2.3 \times 10^{36} \text{ ergs s}^{-1}$ ; they suggested that a search for a pulsar in N157B should commence. Chu et al. (1992) determined the boundary of the SNR based on kinematic information and suggested that N157B is another example of an off-center SNR expanding into a pre-existing superbubble and that the SNR may be interacting with a dark cloud on its southern edge; this dark cloud may shadow the soft X-ray emission from the SNR.

A detailed *ROSAT* and *ASCA* study of N157B was presented by Wang & Gotthelf (1998a). Their spectrum is dominated by a non-thermal component with power law slope  $\Gamma \sim 2.5$ , although there are hints of emission lines below 2 keV that they attributed to a thermal plasma from the SNR with  $kT = 0.4\text{--}0.7 \text{ keV}$ . *ROSAT/HRI* revealed a comet-shaped central nebula that dominates the X-ray emission, explained as a synchrotron nebula from a pulsar moving through the ISM at a rate of  $\sim 1000 \text{ km s}^{-1}$ , although no pulsed emission was apparent in these data.

The long-awaited detection of PSR J0537–6910 in N157B, with a period of 16 msec and a power law photon index of  $\Gamma = 2.6$ , came serendipitously from an *RXTE* observation of SN1987A (Marshall et al. 1998) and was soon confirmed by *BepoSAX* (Cusumano et al. 1998). A slightly later *ROSAT/HRI* detection provided an arcsecond position for the pulsar (Wang & Gotthelf 1998b). This is the shortest period known for a pulsar as-

sociated with a SNR. This pulsar remains undetected in the radio (Crawford et al. 2005) and no unambiguous optical counterpart has been found, even with deep *HST/ACS* imaging (Mignani et al. 2005).

The thermal emission component in N157B’s spectrum is confirmed by *XMM* (Dennerl et al. 2001), also confirming N157B as a composite SNR, containing a Crab-like synchrotron core with  $\Gamma = 2.83$  (Dennerl et al. 2001) surrounded by a thermal shell. *Chandra* has observed N157B directly with both the HRC (Wang et al. 2001) and ACIS-S using subarray readout (ObsID 2783, PI Wang). With the HRC data, Wang et al. (2001) were able to pinpoint the position of the pulsar to  $< 1''$  and to resolve a compact pulsar wind nebula at the “head” of the comet-shaped nebula seen by *ROSAT* (Wang & Gotthelf 1998a). This  $\sim 2'' \times 7''$  feature is centered on the pulsar and oriented perpendicular to the larger cometary nebula. Wang et al. (2001) explain this feature as a toroidal pulsar wind nebula confined by the bow shock from the supersonic motion of the pulsar and depositing its energy in the trailing cometary nebula.

## 2.3. Past Work on This *Chandra* Observation

Our short *Chandra/ACIS-I* observation of 30 Dor (described in detail below) was one of the first observations made by *Chandra* and was part of the ACIS Team’s Guaranteed Time Observation program. We have reported preliminary results from this observation at several meetings (Townsley et al. 1999, 2000b, 2002a) and have used it to estimate the position of PSR J0537–6910 in the N157B SNR (Mignani et al. 2005). With this study we finally are able to provide a detailed analysis of this observation, after several years’ worth of code development and special analysis techniques were implemented. Our custom tools are also useful for analysis of other *Chandra* fields, so we have made them publicly available (see §3).

This dataset has also been studied by other groups. Recently, Lazendic et al. (2003) proposed two new SNR candidates in the 30 Dor nebula based on radio continuum maps obtained with the *Australia Telescope Compact Array*, although the *Chandra* data showed no X-ray enhancements associated with these regions. Chu et al. (2004) examined this claim and concluded, based in part

on the absence of associated X-ray emission, that these small radio sources are not SNRs; rather one is likely a young star-forming region and the other a molecular cloud.

Portegies Zwart et al. (2002) found 20 mostly pointlike sources in the inner  $11' \times 11'$  of the ACIS-I field of view and studied 11 of those in the central region, within  $100''$  from the core of R136. They matched these sources with known early-type (WR and O) stars, some known to be binaries, and concluded that they are bright in X-rays because they are all probably colliding-wind binaries. Stevens & Hartwell (2003) included a spectral analysis of unresolved X-ray emission around R136 in their study of the properties of super star clusters. Some unspecified number of point sources was removed from the inner  $16''$  of R136, then the remaining X-ray emission was fit with a thermal plasma model, resulting in fit parameters of  $N_H = 4.2 \times 10^{21} \text{ cm}^{-2}$ ,  $kT = 2.1 \text{ keV}$ , and absorption-corrected luminosity  $L_X = 5.5 \times 10^{34} \text{ ergs s}^{-1}$ . In Paper II we show that more X-ray point sources in R136 are discernable in this dataset than these two papers considered; their results would change somewhat if these faint sources were included in their analyses.

Since our observation included the two off-axis ACIS-S chips S3 and S4, we were able to image an  $8'.5 \times 17'$  region to the southwest of 30 Dor, featuring SN1987A, the large superbubble 30 Dor C, and the Honeycomb Nebula (see Figures 1 and 2). As mentioned above, the *XMM-Newton* first-light image was centered on this field and gives much better spatial and spectral information on these structures than this short ACIS exposure (Dennerl et al. 2001). The X-ray brightening of SN1987A has been monitored by *Chandra* since early in the mission; see Park et al. (2005) and references therein. 30 Dor C, an unusual non-thermal X-ray emitter, has been studied with *Chandra* (Bamba et al. 2004) and *XMM* (D. Smith & Wang 2004). Given these better datasets and existing studies, we will not include detailed analysis of these sources in this paper.

The results we present below represent only one step in the high-resolution characterization of X-rays from the 30 Dor region. A 100 ks *Chandra* ACIS-I observation of 30 Dor is scheduled for later this year; it should give a  $\sim 5$ -fold improvement in sensitivity and signal over the results reported

here.

### 3. *CHANDRA* OBSERVATIONS AND ANALYSIS

#### 3.1. Instrumental Set-up

We observed 30 Dor and its environs for  $\sim 26$  ks with ACIS-I on 1999 September 21–22. R136 was placed at the aimpoint. The focal plane temperature at this early point in the mission was  $-110\text{C}$  to facilitate water outgassing; it was later reduced to  $-120\text{C}$  to improve detector performance. This higher focal plane temperature causes the effects of radiation damage to the frontside-illuminated CCDs in the ACIS-I array to be particularly pronounced (Townsley et al. 2002b). For example, the spectral resolution at 1.5 keV varies across the device from  $\sim 75$  eV FWHM at low CCD row numbers to  $\sim 170$  eV at high row numbers. Unfortunately, the aimpoint of the ACIS-I array falls near the top of the I3 CCD, so spectral resolution for the sources in R136 is particularly bad. A summary of the observations is given in Table 1.

The first  $\sim 1$  ks of the observation (Observation Identification or “ObsID” 22) was made in the usual “timed event, faint” mode, with  $3 \times 3$  pixel events, 3.2 s CCD frames, and the Spectroscopy Array (ACIS-S) CCDs S2 and S3 operating in addition to the ACIS-I devices. The remainder of the observation (ObsID 62520) was taken in “timed event, very faint” mode ( $5 \times 5$  pixel events) using the “alternating” readout mode with a 10:1 cycle; every ten CCD frames were exposed for 3.3 s, then every eleventh frame had a short 0.3 s exposure. The data processing pipeline divides these short and long frames from ObsID 62520 into separate event lists. In order to image interesting structures near the 30 Dor field, ACIS-S CCDs S3 and S4 were operational for this observation.

We chose to use the ACIS camera’s alternating-exposure mode because the 30 Dor field contains PSR J0537–6910, a bright 16 ms pulsar (Marshall et al. 1998). Although it is imaged  $\sim 7'$  off-axis, we knew that it would still suffer from photon pile-up in regular-length CCD frames, so we included the short frames to try to mitigate pile-up on this source. In hindsight, this was not an ideal approach, as there are too few photons in the short frames to provide much information on PSR J0537–6910 and the use of alternating mode

this early in the mission caused problems for the data processing pipelines, resulting in absent or incorrect Good Time Interval (GTI) tables, incorrect keyword values, and other complications.

For this analysis, we used Version 3 of the pipeline processing (created 26 July 2001), which has correct GTI tables. Even this third version of the data still contains some errors though; for example, the EXPOSURE and LIVETIME keywords in the 0.3 s event list of ObsID 62520 are incorrect. After recalculating these quantities for each CCD and correcting the header keywords in the event list, a total of  $\sim 200$  s of data taken with 0.3 s CCD frames is obtained.

### 3.2. Data Analysis

Starting with the Level 1 event lists, the data were reduced using our standard methods, as described in Townsley et al. (2003) and Getman et al. (2005), using *CIAO* 3.0.2. *Chandra* source positions were determined from the source-finding routine *wavdetect* (Freeman et al. 2002) run on a  $2 \times 2$ -pixel binned image of the hard band (2–7 keV) data from the “long” observations in ObsID 62520; data below 2 keV were excluded to minimize the contamination of source positions by the soft diffuse emission that pervades the field. ObsID 62520 was registered to the astrometric reference frame of 2MASS using 4 matches. Offsets were  $+0.95''$  in RA,  $+1.0''$  in Dec.

The *Clean55* algorithm<sup>2</sup> developed by Alexey Vikhlinin was used to flag events in ObsID 62520; these flagged events were removed to suppress background for source-finding and image generation, but this flag can also erroneously remove events from the cores of point sources so it was not applied in spectral analysis. Due to a strong background flare caused by particles generated by solar activity, ObsID 62520 has some telemetry saturation that only affects the S3 chip, from frame  $\sim 7248$  ( $\sim 24300$  sec) to the end of the observation. Background flares affected CCD S3 both early and late in the exposure and those times were filtered from the S3 data; other CCDs were unaffected by these flares. The *CIAO* “destreaking” algorithm by John Houck<sup>3</sup> was applied to CCD8 to suppress noise on that device.

---

<sup>2</sup><http://hea-www.harvard.edu/~alexey/vf.bg/vfbg.html>

<sup>3</sup><http://asc.harvard.edu/ciao/threads/destreak/>

We did not adjust the astrometry of ObsID 22 due to only two 2MASS matches and inconsistent, small offsets with those matches. Although we would normally not remove the event position randomization added in the standard data processing pipeline for such a short observation, it was removed for ObsID 22 in order to combine these data with ObsID 62520. S3 was experiencing background flares for the duration of this short observation. Given that and the short amount of total integration time for the area covered by CCD S2, only the ACIS-I array component of this observation was merged with ObsID 62520.

For ObsID 62520, individual CCD columns were examined in chip coordinates using our *Event Browser* tool<sup>4</sup> (Broos et al. 2000) to search for additional hot pixels and columns that were not part of the pre-defined bad pixel file and to establish the energies of those noise events. At  $-110\text{C}$ , there are many more hot columns (exhibiting extra noise below 1 keV) than at  $-120\text{C}$  (the focal plane temperature used from January 2000 to the present), especially on CCD S4. Those events were removed from both ObsID 62520 and ObsID 22 using CIAO 2.3 because the necessary “exclude” syntax (to remove only certain energies from specified spatial coordinates) was not working correctly in CIAO 3.0.2. Although the effects of these deleted events cannot be included in the exposure map (because only events below certain energies, not all events from a given column, were removed), we chose to suffer this slight calibration error rather than to retain the noisy events because they become especially pronounced and distracting in smoothed soft-band images.

Both datasets were corrected for charge transfer inefficiency (CTI) using the Penn State CTI corrector, which was originally developed specifically to address the CTI problem for this dataset<sup>5</sup> (Townsley et al. 2000a, 2002b), due to our interest in spectral analysis of the many point-like and diffuse structures in this field. It remains the only CTI corrector available for the backside-illuminated CCD S3 and for all ACIS data taken at a focal plane temperature of  $-110\text{C}$  (where CTI is worse than at  $-120\text{C}$  for frontside-

---

<sup>4</sup>Code available at <http://www.astro.psu.edu/xray/docs/TARA/>

<sup>5</sup>Details, source code, and calibration products for CTI correction are available at <http://www.astro.psu.edu/users/townsley/cti>.

illuminated CCDs, as mentioned above). Custom response matrices (RMFs) and quantum efficiency uniformity (QEU) files were generated to facilitate spectral fitting for  $-110\text{C}$  data (Townsley et al. 2002c). We also refined the event positions in both datasets using the subpixel positioning algorithm developed by Koji Mori<sup>6</sup> (Mori et al. 2001; Tsunemi et al. 2001).

The reduced event lists were then merged and the exposure maps added. A *status=0* filter was applied to create an event list appropriate for source searching and image generation. The data were once again examined in *Event Browser*, showing that the best energy range to consider for imaging studies is 350–7300 eV; the lower limit retains events below 500 eV that are clearly from the diffuse superbubble structures in the field while limiting low-energy noise, while the upper limit is set just below the instrumental Ni  $\text{K}\alpha$  line, which marks the beginning of enhanced high-energy background.

Next we conducted a multistage process for identifying and extracting photons of unresolved sources that is described in detail in Paper II. It involves source identification using a wavelet transform and a maximum likelihood image restoration algorithm. Point source events for the final list of 180 sources were then extracted using PSB’s IDL-based code *ACIS Extract* (Broos et al. 2002) developed to treat complicated fields with multiple point-like and diffuse components<sup>7</sup>. For analyzing the diffuse components in the 30 Dor field, the only point source properties required are their locations and extraction regions; these are provided in Tables 1 and 2 of Paper II. These are used to construct a point source mask and a source-free dataset suitable for analysis of diffuse emission.

We used a mask produced by the *ACIS Extract* tool *ae\_optimal\_masking* which identifies regions where the expected surface brightness from the calibrated point sources is larger than one half the smoothed observed local background. These point source masks are illustrated in Figure 3, which shows the I-array exposure map for ObsID 62520. Chip gaps and bad columns are seen as areas of reduced exposure, while the small white regions dis-

tributed across the field and concentrated in the center show areas of zero exposure representing areas that were masked to exclude point sources. This figure also illustrates that the *Chandra* PSF is a strong function of off-axis angle; most of the X-ray point sources in the field are concentrated in R136 (field center), yet the sharp PSF on-axis leads to relatively little area removed for diffuse emission studies there.

Extraction regions for a variety of diffuse structures were then defined by hand, based on the apparent surface brightness in a smoothed, sources-removed image. Spectra, backgrounds, ARFs, and RMFs for all point sources and diffuse structures were constructed by *ACIS Extract* and used for both automated and interactive spectral fitting using Keith Arnaud’s *XSPEC* fitting package (Arnaud 1996) and *XSPEC* scripts provided by Konstantin Getman.

#### 4. GLOBAL PROPERTIES OF THE X-RAY EMISSION

We start by describing the large-scale features revealed by this ACIS observation. Figure 1 shows the soft-band image of 30 Dor created with the adaptive-kernel smoothing tool *csmooth* in *CIAO* (a translation of the *asmooth* code by Harald Ebeling). This smoothed image emphasizes the soft diffuse structures, mapping red to the spectral range 500–700 eV, green to 700–1120 eV, and blue to 1120–2320 eV. The reduced, full-field, full-band binned data are shown in Figure 2. The event data were binned into  $8'' \times 8''$  pixels to create this image. Some well-known objects are labeled, as are the ACIS CCDs used in this observation. Areas of reduced exposure between the CCDs are clearly visible, as is the extensive diffuse X-ray emission present in this field. Several famous structures are imaged far off-axis on the S3 and S4 CCDs.

##### 4.1. X-ray Morphology

In these images we see a bright concentration of hard X-ray events associated with the R136 star cluster at the center of the ACIS-I array and fainter emission from several other well-studied stellar objects, mostly WR stars (see Figure 1 in Paper II). The bright SNR N157B is a distinct, extended feature to the southwest of the main 30 Dor complex. It is the hardest source in the

<sup>6</sup>Code available at <http://www.astro.psu.edu/users/mori/chandra/>

<sup>7</sup>The *ACIS Extract* code is available at [http://www.astro.psu.edu/xray/docs/TARA/ae\\_users\\_guide.html](http://www.astro.psu.edu/xray/docs/TARA/ae_users_guide.html).

field due to non-thermal emission from its central pulsar and synchrotron nebula, but the larger SNR softens with distance from the pulsar. A number of widely-distributed compact X-ray sources are scattered across the field; some were seen in previous X-ray studies (§2). The hard sources are probably mostly background AGN (see Paper II).

By far the dominant features, however, are the large diffuse structures associated with the superbubbles produced by existing and past OB associations and their supernova events. These structures were well-known from *Einstein* and *ROSAT* studies, as outlined in §2 (see especially the HRI data in Wang 1999), but higher on-axis spatial resolution of *Chandra* and the ACIS camera's intrinsic spectral capabilities reveal a new level of complexity. The center of the field is complicated by crossing ACIS-I chip gaps but clearly contains some of the hardest emission in the field, due to the R136 cluster, R140, and R145. Faint, softer diffuse emission appears to pervade the central region. Just northwest of R140 (due west of R139) is a bright, medium-soft clump  $\sim 1'$  in size.

Shell 1 in Figure 2 contains several point sources but is dominated by a bright, medium-energy clump of diffuse emission roughly  $1'.5 \times 2'$  in size. An ACIS-I chip gap bifurcates this feature, so the two-lobed structure it shows in Figure 1 is largely an artifact (see Figure 1 in Wang 1999). Shell 2 is shown as a larger structure in Figure 2 than originally defined (Meaburn 1984; Wang & Helfand 1991a) because the kinematic study of Chu & Kennicutt (1994) showed that the expanding shell is larger than the morphological Shell 2 identified in an  $H\alpha$  image (Meaburn 1984). It is edge-brightened in X-rays, with a large central void and a sharp boundary along its southeast edge. There are small clumps of emission around its periphery, many of which are consistent with point sources. Its faint emission is harder than the other shell structures in the 30 Dor nebula. At its upper center is an interesting comet-shaped feature showing substantial spectral complexity, with a soft point source at its head.

Shell 3 is also largely edge-brightened, quite faint and soft around its periphery but with a harder, nearly-complete, clumpy central ring about  $2'.5$  in diameter (hereafter called the “West Ring”). This ring structure also shows spectral complexity, appearing harder on its western

half. A faint, small clump is nearly centered on this ring, but it is too large and diffuse to be a point source. The  $\sim 20$  Myr old stellar cluster Hodge 301 (Grebel & Chu 2000) sits at the northeast edge of this ring, but we do not resolve any X-ray point sources in it. Shell 3 encompasses two dark voids, one on either side of its central ring.

Shells 4 and 5 are both distinctly soft and bright, and differ from the other shells in that they appear center-filled rather than edge-brightened. Shell 5, unfortunately, has a chip gap running all the way through its long dimension, so some of the structure we see may be affected by that. Both it and Shell 4 are spectrally uniform and similar to each other. Shell 5 is quite clumpy, with a bright lower clump about  $1' \times 2'$  in size containing the WR star R144 and a string of smaller, fainter clumps populating its interior.

The off-axis ACIS-S CCDs appear to be pervaded by soft, faint diffuse emission. (Small point-like features around the edges of this field seen in Figure 1 are smoothing artifacts.) The most striking feature here is the superbubble 30 Dor C, seen as a nearly complete ring of clumpy emission spanning S3 and S4; its western half is very hard in X-rays due to strong non-thermal emission (see §2). SN1987A is the bright point source on S4; its light is spread across a region more than an arcminute in size due to *Chandra*'s broad PSF at this large off-axis angle ( $> 20'$ ). The bright, soft feature at the lower center of S4 is the Honeycomb SNR; superposed on it appears to be a large ring of soft, diffuse emission that arcs to the north and east of the Honeycomb. Such faint, far off-axis features are more clearly seen in the *XMM* first-light image (Dennerl et al. 2001).

#### 4.2. Other Views

Given the great variety of diffuse X-ray structures apparent in this observation, it is worthwhile to find new ways to highlight them. Figure 4 shows a color composite of three adaptively-smoothed images (from PSB's adaptive kernel smoothing tool *adaptive\_density\_2d*, Townsley et al. 2003) where the 180 point sources in the field have been removed and the resulting “holes” smoothed over. The images were made in three soft bands, 350–700 eV, 700–1100 eV, and 1100–2200 eV, similar to the bands used to create Figure 1. They were combined to show the spectral variety that must

be present in the diffuse structures, even on spatial scales too small for us to extract and fit spectra to demonstrate this variety; the intensities were set to emphasize faint diffuse features.

This smoothing technique has the advantage (over that used in Figure 1) that it does not create artifacts around the edges of the field, although the overall appearance is more blurry. We think that the best impression of the field comes from actively comparing these two renderings. For example, the West Ring in Shell 3 is much more clearly portrayed by Figure 1, but there are two small, faint loops ( $< 2'$  in diameter) on its north and east edges that are only visible in Figure 4. We do not have enough data to know whether or not these features are real.

With the point sources gone from Figure 4, we are free to concentrate on the diffuse structures. Here the outer loop in Shell 3 is more pronounced, as are other faint diffuse features, especially on the S-array CCDs. Another intriguing small loop not apparent in Figure 1 is seen in the eastern half of Shell 2, visible as a green arc  $\sim 1.5'$  across just above a bright green knot in the sharp lower edge of Shell 2. Again, only more data will allow us to understand this feature in detail.

### 4.3. Spectra

For comparison with more distant GEHRs, Figure 5 shows spectra of large-scale regions of X-ray emission on the ACIS-I array and *XSPEC* fits. Fit results are given in Table 2. Column 1 lists the various composite regions on which spectral fits were performed; rows 1–4 correspond to the fits shown in Figure 5. Column 2 gives the number of counts used in the fit. Columns 3–8 give the spectral fit parameters, while columns 9–12 show the elemental abundances relative to solar values from the *vapec* thermal plasma model (R. Smith et al. 2001) for elements that required  $Z > 0.3Z_{\odot}$ . Columns 13–17 give the X-ray luminosities based on the spectral fits for a variety of wavebands, with and without correction for absorption.

Column 8 shows that many of these fits are not formally acceptable (the reduced  $\chi^2 > 1.1$ ). This is due mainly to the large number of degrees of freedom, which is in turn due to the large number of events in these spectra; while in principle more events should allow the reduced  $\chi^2$  to approach

unity as signal-to-noise improves, in practice systematic errors in the ARF and RMF become more important and the reduced  $\chi^2$  remains high. The fits in Figure 5 show that the spectral models used in Table 2 characterize the data quite well in spite of the formally unacceptable fit; a more complicated model (such as an additional thermal plasma component) does not improve the fit.

Figure 5a illustrates the global spectral fit for all components of the main 30 Dor nebula as outlined in Figure 2, including point sources, the SNR N157B, its pulsar, and its cometary nebula. The spectrum is fit with a single absorbing column via the *wabs* model (Morrison & McCammon 1983), which assumes solar abundances for the absorbing material, and a spectral model consisting of two components: a variable-abundance thermal plasma and a power law. The average absorption is a factor of 2 smaller than the *ROSAT* result (Norci & Ögelman 1995), although the plasma temperature is similar. Norci & Ögelman (1995) do not state what abundances they assume for the absorbing material and Mignani et al. (2005) note that abundances of  $0.4Z_{\odot}$  give  $N_H$  values a factor of two higher than those for solar abundances when fitting the spectrum of PSR J0537–6910, so perhaps different assumptions regarding the metallicity of the intervening material account for this discrepancy in the average absorption. The ACIS soft-band intrinsic (absorption-corrected) luminosity for the main 30 Dor nebula is a factor of 2.5–5 smaller than the *ROSAT* 0.1–2.4 keV estimate (Norci & Ögelman 1995).

Figure 5b covers the same region of X-ray emission as Figure 5a minus the N157B SNR (a composite spectrum of the SNR is shown in §6.2). Since N157B is quite bright and contains substantial non-thermal emission that would not necessarily be present in a more distant GEHR unless it contained a recent supernova, removing it from the overall spectrum of 30 Dor might yield a more typical GEHR spectrum. The *wabs\*(vapec + powerlaw)* fit is actually quite similar to that in Figure 5a, with nearly the same  $N_H$ ,  $kT$ , and plasma abundances as that fit, but a steeper power law slope. This shows that, although the non-thermal N157B pulsar and cometary nebula are bright compared to other point sources in the field, the overall spectral shape of the GEHR is still dominated by a soft thermal plasma with fairly

simple spatially-averaged spectral properties—no prominent lines are present and there is no obvious need for multiple plasma components or absorbing columns to fit the composite spectrum. The only indication of the presence of the pulsar is at high energies, where it flattens the power law component of the fit.

The same extraction region is used for Figure 5c as was used in Figure 5b, but now the 158 point sources that this region contains have been removed from the spectrum. The composite spectrum of those point sources is shown in Figure 5d. With only the diffuse emission component remaining in Figure 5c, the power law is no longer needed in the spectral model; rather the emission can be represented by a single, slightly hotter thermal plasma with enhanced abundances. The composite point source spectrum in Figure 5d requires a hotter thermal plasma and a flatter power law; it constitutes less than 10% of the full-band emission in this region but dominates the hard-band (2–8 keV) emission by a factor of 3 over the diffuse component.

These fits suggest that unresolved GEHRs in more distant galaxies might appear as soft, moderately luminous ( $L_X \sim 10^{36}$  ergs s $^{-1}$ ) X-ray sources, quite distinct from harder and often brighter ( $L_X \sim 10^{37}$ – $10^{40}$  ergs s $^{-1}$ ) X-ray binaries. Distinguishing GEHRs from individual SNRs, though, is probably only possible for young SNRs, which might present hotter thermal plasmas or occasionally non-thermal emission and may have prominent line features. Even though the N157B SNR is quite young, it does not show prominent lines and, when averaged with the emission from the rest of 30 Dor, it is not bright enough to harden the composite spectrum. If its non-thermal central components were absent, it would not be spectrally distinct from the other diffuse structures in 30 Dor. This is illustrated in the spectral fitting presented in §5 and §6 below.

Despite its complex spatial morphology, 30 Dor’s integrated thermal emission has simple spectral properties: it is well-fit by a single-temperature plasma with  $T \simeq 4$  MK, roughly solar line strengths, and a single absorbing column density. We will see in §5.2 that a considerable variety of plasma temperatures and absorbing columns are present on small spatial scales. In the ACIS soft band (0.5–2 keV), the X-ray luminosity comes

primarily from the diffuse structures, which are brighter by an order of magnitude than the point sources. Above 2 keV, though, the diffuse emission disappears and the integrated emission is dominated by the point sources. Paper II demonstrates that this point source emission is itself dominated by a few bright sources; one third of the counts that compose the spectrum in Figure 5d come from a single source (probably a colliding-wind binary, Portegies Zwart et al. 2002).

## 5. THE X-RAY SUPERBUBBLES

### 5.1. Morphology

As outlined in §4.1, the five plasma-filled superbubbles first defined by Wang & Helfand (1991a) from *Einstein* observations of 30 Dor appear to be much more complicated structures in these ACIS images, exhibiting knots, wisps, loops, and voids with a range of surface brightnesses and X-ray colors. In some cases the X-ray morphology may be affected by the clumpy molecular clouds in the region (Johansson et al. 1998), the shreds of the material from which R136 formed. This neutral material may shadow soft X-rays; comparing CO cloud locations from Johansson et al. (1998) to our smoothed images, this effect may account for some of the X-ray voids close to R136, although probably not the larger, more distant voids seen in Shells 2 and 3.

Some X-ray regions show distinctive sharp edges, such as the long north-central bubble comprising Shell 5 and the long arc stretching across the southeast edge of Shell 2. Other regions such as the large loop cut off by the northwest edge of the ACIS-I array have softer edges that seem to blend into faint, larger-scale diffuse emission. The two bubbles of Shells 4 and 5 running almost due north and south of R136 appear quite red in Figures 1 and 4, perhaps implying that they are less absorbed than other parts of the field or are filled with cooler gas. They are also distinctly center-filled, while other superbubbles appear as loops with central voids. The ACIS-S structures 30 Dor C and the faint loop that arcs to the northeast of the Honeycomb SNR are good examples of such loops, but the main 30 Dor complex shows them as well.

In the hot thermal plasma models that we use for spectral fitting of these data (see §4.3), most

of the emission between 0.5 and 2 keV comes from a large number of blended spectral lines, with only a small remainder caused by thermal bremsstrahlung. In order to understand the morphology of 30 Dor’s superbubbles and its energy dependence, Figure 6<sup>8</sup> shows narrow-band smoothed images of the full ACIS field centered on some of the most prominent spectral lines in the thermal plasma models, specifically those often seen in SNRs, following *Chandra* studies of Magellanic Cloud diffuse nebulae by Behar et al. (2001) and Nazé et al. (2002). The continuum emission dominates the highest-energy image ( $\sim 65\%$ ) but contributes only  $\sim 10\text{--}30\%$  to the other narrow-band images.

While small-scale changes between narrow-band images should be viewed with caution due to limited photon statistics, it is clear that all of these images hint at the presence of complex fine spatial structure and that the morphology of large-scale structures changes substantially with energy. A good example of this is 30 Dor C, which seems to emerge out of faint, unorganized swaths of soft emission to coalesce into the well-defined hard loop that we see in broad-band images. The large, soft superbubble at the south-center of the ACIS-I array (Shell 4) and the loop containing the Honeycomb SNR are prominent in the softer images, but fade above 950 eV. Conversely, the sharp southeast ridge seen on CCD I1 (edge of Shell 2) becomes more prominent at higher energies and the void to its northwest appears to be filling in, with no void left in the 1780–1940 eV image. Smaller-scale knots and wisps near the center and west-center of 30 Dor also come and go with energy, with some prominent in the softer panels and others bright at higher energies.

These images show that substantial spectral variation exists in the 30 Dor superbubbles but do not by themselves reveal whether the variations are produced by spatial changes in absorption columns, plasma temperatures, abundances, or other phenomena. To investigate this question,

<sup>8</sup>These images (point sources removed) were made with the *adaptive-density-2d* procedure in *ACIS Extract* using the smoothing scales from a broadband (350–2000 eV) image, so that all narrow-band images have the same smoothing scales. To account for the fact that each narrow-band image was made from a different number of events, each image was normalized by its median intensity, then all were scaled the same in the display.

we divide the diffuse emission on the ACIS-I array as shown in Figure 7. These regions were chosen primarily on the basis of apparent surface brightness of the diffuse emission and overall morphology of the 30 Dor complex, so they form a phenomenological rather than a physical parameterization of the X-ray emission. We emphasize that they were not chosen by considering the morphology of 30 Dor in any other waveband; this will become relevant later in this paper.

The three large green polygons labeled “B” are the regions used to obtain the background spectrum used in all spectral fitting of diffuse regions described in this paper. From *XMM* data of this region (Dennerl et al. 2001) and *ROSAT* maps of the LMC (e.g. Points et al. 2001; Sasaki et al. 2002), we know that these regions contain faint diffuse emission, but this may be the most appropriate background to use, as the whole field may well be pervaded by such faint diffuse emission.

The regions in Figure 7 are best understood by considering them hierarchically by size, starting with the outermost, largest regions and working inward and to smaller sizes. The large red contour outlines the region used earlier for the global spectral properties of 30 Dor. The six white regions define large-scale diffuse structures, including the N157B SNR. Region 1 encompasses the brightest emission from the whole nebula, including regions 3, 12, 16, 24, n8, and the central polygon that these regions abut. Region 2 is the perimeter between region 1 and the outer red contour, also excluding region 18. The five purple contours define “voids,” or areas of low apparent surface brightness. Two central green regions (9 and 10) outline relatively bright central structures. Contained within these large-scale regions are smaller regions defining locally bright areas, in blue, yellow, cyan, and red. A cyan contour in the far northeastern corner (region 23) defines an area of faint diffuse emission known from *ROSAT* observations (Points et al. 2001). A series of annular regions (n0–n7) is used to explore the spectral properties of the N157B SNR; §6 gives more detail.

After choosing these extraction regions based on the X-ray apparent surface brightness in our *Chandra* images, we compared them to the  $\sim 100$  ks *XMM* first light image in Dennerl et al. (2001), which contains the western half of the main 30 Dor nebula. This image closely matches the

*Chandra* data, showing very similar diffuse X-ray structures, and justifies our choice of extraction regions even for faint features such as the outer loop in Shell 3 that we delineate as region 18, soft features such as regions 3 and 4 that fill Shell 4, and the X-ray voids in regions 19, 20, and 21.

## 5.2. Spectra

The spectral variety in these diffuse regions is shown in Table 3. Column 1 gives the identifier of the regions shown in Figure 7. Column 2 gives the net full-band (0.5–8 keV) counts in each diffuse region. Spectral fit parameters, allowing for both *vapec* thermal plasma and power law fits, are given in Columns 3–7. Column 8 gives the reduced  $\chi^2$  value for the fit. All elemental abundances were allowed to vary; Columns 9–12 show abundances relative to solar that exceeded the nominal value  $0.3Z_\odot$ . These abundances were not always well-constrained in the fits; in cases where the fit was improved with higher abundances but actual values were not well-determined, they are listed as “hi” in the table. Derived X-ray luminosities are given in Columns 13–16; since the diffuse emission is quite soft in most extended regions (apart from the center of N157B), we report the intrinsic (absorption-corrected) soft-band luminosity as well as the usual intrinsic full-band luminosity. The area subtended by each diffuse region is given in Column 17 and the table is completed by a list of intrinsic soft-band surface brightnesses in Column 18.

Using methods similar to those developed by Jeremy Sanders for study of extragalactic plasmas (e.g. Sanders et al. 2005), we have used thermal plasma fits and the regions defined in Figure 7 to produce maps of  $N_H$ ,  $kT$ , and intrinsic X-ray surface brightness in 30 Dor, as shown in Figure 8. For uniformity, the spectral fits used to make these maps were single-temperature thermal plasmas, so the results are not necessarily the same as those presented in Table 3, where power law components were added for some regions. Characteristics of the largest regions are recorded first and are overlaid by those of smaller regions. This approach has the misleading effect of leaving apparent “rings” around void regions (e.g. regions 15 and 19) where the underlying large-scale fit is not masked by an overlying smaller region.

Although crude, these maps are useful for un-

derstanding the physical state of the plasmas that make up the 30 Dor diffuse emission. For example, region 4 is not intrinsically more luminous than the surrounding region 3, it is just less absorbed and, since it has the same temperature as region 3, its apparent surface brightness is larger. The same explanation applies to region 8. Region 11 is particularly bright, even though it has the same plasma temperature as its surrounding region 10, because it is slightly less absorbed plus it has intrinsically higher surface brightness. Regions 25 and 26 suffer more absorption than the surrounding region 24 and have cooler plasma temperatures, but they stand out because they have higher intrinsic surface brightness. Regions 18 and 19 suffer similar high obscuration and have the same cool plasma; region 19 appears as a void because it is intrinsically fainter than its surrounding region 18, which is only visible to us in regular images because it has relatively high intrinsic surface brightness. Region 22 has similar obscuration and plasma temperature, but appears as a void because it lacks this enhanced intrinsic brightness.

Particularly unusual is region 15, which has high obscuration and low intrinsic surface brightness so it appears to us as a void, but it has the highest plasma temperature in the nebula. Region 5 is also interesting, exhibiting a low temperature and relatively high obscuration, but it is very bright in regular images due to its intrinsic brightness, one of the largest in the nebula. Of even higher intrinsic brightness, though, is region 7, yet it is much less noticeable because of its large obscuration. The intrinsically faint and soft emission in region 23, probably associated with more eastern structures rather than with 30 Dor itself, is visible only because of its minimal obscuration.

In order to get enough counts for reliable spectral fitting, the regions used here average over many tens of square parsecs. From the complex energy variations seen in Figures 1, 4, and 6, it is quite possible that each region averages over many distinct plasma components, with different pressures, densities, temperatures, absorbing columns, and possibly even different abundances. Study of such features and their energetics will be possible when longer ACIS exposures of the region are made.

## 6. THE SUPERNOVA REMNANT N157B AND PSR J0537–6910

### 6.1. Morphology

The *Chandra*/HRC (Wang et al. 2001) and ACIS images of the composite SNR N157B are incremental improvements to the *ROSAT* data, which also showed a comet-shaped nebula embedded in a diffuse remnant, suggesting that the neutron star received a kick in the supernova blast and is plowing through the surrounding ISM (Wang & Gotthelf 1998a). Smoothed, soft-band and hard-band ACIS images of N157B are shown in Figure 9. The soft-band image (Figure 9a) shows the point source extraction regions outlined in red; the hard-band image (Figure 9b) additionally shows the concentric diffuse extraction regions n7–n0 as defined in Figure 7 and Table 3. The extraction region for the pulsar is shown in white.

The ACIS soft-band smoothed image shows diffuse emission from N157B extending somewhat farther than that shown in the HRC data (Wang et al. 2001, Figure 1), giving dimensions for the X-ray SNR of  $\sim 3'.3 \times 3'.5$ , or roughly 50 pc in diameter. The soft X-ray emission might be partially shadowed along the southern edge of the SNR by the dark cloud described in Chu et al. (1992). The hard X-ray emission in Figure 9b, which would not be shadowed because it penetrates such material, does not appear to extend into this region, though. Thus it does not appear that the SNR extends behind the southern dark cloud.

Figure 10 shows ACIS images of the embedded cometary nebula and pulsar. The SNR is imaged 6'.9 off-axis, where the PSF is  $\sim 5'' \times 10''$  in size (shown in white in Figure 10a). The central source is still quite centrally peaked and sharp enough that photon pile-up affects its spectrum. Since it is immersed in its pulsar wind nebula and may have further corruption from the surrounding cometary nebula and SNR, our estimate of the pulsar’s power law slope ( $\Gamma = 2.0$ ) should be considered qualitative. Mignani et al. (2005) estimate  $\Gamma = 1.8$  for the pulsar using an ACIS subarray observation that minimizes photon pile-up for the pulsar and images it on-axis, so the small PSF limits the contamination from diffuse structures around the pulsar.

Figure 10b shows the maximum likelihood re-

construction of Figure 10a, using the PSF of the pulsar for the reconstruction of the whole field. We recover an image very similar to the on-axis *Chandra*/HRC images in Wang et al. (2001): the pulsar is a circular point source centered on its pulsar wind nebula and a bright,  $\sim 4'' \times 7''$  region of emission is oriented perpendicular to the larger, trailing cometary nebula. Although this image is not useful for spectral analysis, it is reassuring that even a simple reconstruction algorithm can recover information far off-axis, for sufficiently bright sources.

### 6.2. Spectra

Figure 11a shows the spectral fit for the entire N157B SNR (labeled in Figure 2 and seen as region n8 in Figure 7), including its pulsar (suffering from moderate photon pile-up with  $\sim 0.9$  counts per frame), its pulsar wind nebula, and the surrounding cometary nebula. Fit parameters are given on the last line of Table 2. Using the same spectral model as for Figure 5a and b, we obtain the same  $N_H$  but a hotter thermal plasma. Some elements require abundances  $> 0.3Z_\odot$  but are not well-constrained.

Our thermal plasma fit results are quite similar to the *ROSAT* results (Wang & Gotthelf 1998a), but the power law component is substantially flatter than the results given by other X-ray observations of N157B (see §2.2). Since N157B is a young SNR, we also characterized its spectrum with a variable-abundance non-equilibrium ionization model, using the *XSPEC* model *vnei + powerlaw*. The fit was essentially the same as the thermal plasma fit described above, with  $kT \sim 0.9$  keV and  $\Gamma = 2.2$ , but the fit parameters were not as well-constrained as those for the thermal plasma fit.

Removing all the point sources from this region leaves the diffuse emission associated with the SNR (Figure 11b). Its spectral fit parameters are listed under region n8 in Table 3. The cometary nebula associated with the pulsar contributes the power law component of the spectrum. The thermal emission averaged over the whole SNR is quite soft and possible emission lines of Ne and Mg are seen. While our fit results are consistent with the *XMM* results for the thermal component and overabundances of Ne and Mg are consistent with *XMM*’s discovery of emission lines (Dennerl et al.

2001), our power law slope is slightly flatter than the  $\Gamma = 2.8$  result from *XMM* (Dennerl et al. 2001), even though our fit excluded the pulsar. Dennerl et al. (2001) note that, if N157B is similar to the Crab Nebula, we would expect a difference between the core power law slope and that for the entire nebula of  $\sim 0.5$  due to synchrotron losses. This is seen in our *Chandra* data, confirming the analogy with the Crab.

The *XMM* value for the absorption (assuming an abundance of  $0.5Z_{\odot}$ ) was  $N_H = 1.9 \times 10^{22} \text{ cm}^{-2}$ , more than a factor of 6 higher than our result; the highest absorption we see for any part of N157B is at its core, where our  $N_H$  is still a factor of 3 lower than the *XMM* value. As discussed above, our assumption of solar abundance for the absorption can account for a factor of  $\sim 2$  discrepancy in the measured column, but the cause of the remaining difference in  $N_H$  estimates is unknown. One possibility might be calibration uncertainties in the early *XMM* results or cross-calibration issues between the two observatories.

To study the SNR on finer spatial scales, spectral fits to the annular regions n0–n7 defined in Figure 9 were performed and are given in Table 3. Our spectral fitting confirms the results of Dennerl et al. (2001) and Wang & Gotthelf (1998a) that N157B is a composite nebula, with a thermal plasma showing hints of line emission in the outer regions giving over to synchrotron emission in the bright core. The spectral model in these fits allowed for both a thermal plasma and a power law component, reverting to a single component when an adequate fit could be obtained with just the thermal plasma or the power law model.

We have included two point source extraction regions in this table and show their spectra in Figure 11: p1 contains the pulsar (CXOU J053747.41–691019.8) and p2 (CXOU J053745.61–691011.1) is the point-like component of the cometary nebula found by *wavdetect*. These sources are included because their large off-axis PSFs make it difficult to isolate the point source emission from the surrounding bright diffuse emission, so these point sources include diffuse spectral components. In fact it is not clear in the ACIS subarray observation of N157B that p2 is a point source at all; it is most likely another example of concentrated diffuse emission that is consistent with the ACIS PSF at this large off-axis angle. The spectral fits in Table 3 are not

identical to those in Paper II because the former were performed by hand, while the latter were performed automatically in *ACIS Extract*. The results are consistent to within errors.

Comparing the spectrum of p1 (core, Figure 11c) to p2 (cometary nebula bright point, Figure 11d) and the surrounding bright cometary nebula (n0, the smallest blue annulus in Figure 9b), we see that all three regions are adequately fit by a simple power law, but its slope steepens rapidly away from the pulsar. As we progress through the larger concentric annular regions n1–n7, an additional thermal component is needed for an adequate fit and the power law component apparently becomes very steep. In the outermost annular region (n7), the power law component is no longer necessary. The spectral fits of these annular regions are problematic due to small number counts; there can be interplay between the thermal plasma temperature, the power law slope, and the absorption that can lead to incongruous results, as we see for region n6. Here the power law slope is quite flat, but its normalization is low. The general trend of these annular spectra, though, seems to indicate electron cooling through the steepening power law slope, a transition from non-thermal to thermal spectra with distance from the pulsar, and higher abundances in the SNR, possibly hinting at the presence of spectral lines.

## 7. DIFFUSE STRUCTURES IN THE CONTEXT OF 30 DOR KINEMATICS

From *Einstein* and *ROSAT* data, it has long been known that many of the X-ray concentrations in the 30 Dor superbubbles are spatially associated with high-velocity optical emission line clouds (Chu & Kennicutt 1994, hereafter CK94). These kinematic data are invaluable for sorting out the many overlapping X-ray features seen in the *Chandra* data as well. For example, the large arc that appears to be associated with the Honeycomb SNR is actually not kinematically related to it, but kinematic data indicate that the Honeycomb itself is the result of a cavity supernova explosion. The part of it seen in X-rays is due to the collision of this cavity SNR with an intervening porous gas sheet that could be associated

with its slow-moving giant shell (Chu et al. 1995b; Redman et al. 1999).

We place our bright X-ray features in the context of CK94's echelle study in Table 4. Several prominent X-ray features (identified solely on the basis of their apparent X-ray surface brightness in a smoothed ACIS image, see §5.1) show high velocities in the kinematic data: our West Ring is adjacent to CK94's NW Loop; our region 5 is CK94's R139W; our region 6 is CK94's R136E. This correspondence between high-velocity features and diffuse X-ray emission was noticed and explained by CK94 as X-rays produced in the shocks between high-velocity material and the surrounding slow-moving shells. The *Chandra* data allow us to explore this general idea in more detail, with spatial resolution better matched to that of CK94's echelle data.

### 7.1. X-rays from High-velocity Features

The *Chandra* data show a more complex spatial distribution of X-ray plasmas than that described by Wang (1999), who inferred from *ASCA* data that the diffuse emission was hot in the core of the nebula and cooler in its outer regions. This complex distribution more closely matches the kinematic portrait of the nebula built by CK94, though. Many of the bright X-ray regions that match high-velocity features listed in Table 4 show cooler plasma temperatures than their surroundings (Figure 8b). We interpret this as evidence that these regions are denser due to the high-velocity shocks, hence they are able to cool faster than the surrounding superbubbles.

The high velocities measured near this X-ray-emitting material are more consistent with CK94's interpretation of them as supernova shocks rather than as regions of high mass-loading, as proposed by Wang (1999), although our data do not exclude mass loading as a secondary mechanism for increasing X-ray luminosity in some regions. We would expect this mechanism to be most important in regions where substantial neutral material is known to exist, thus mass loading may contribute to the bright diffuse X-rays seen near the center of the nebula, which contains the remains of the GMC.

Our bright, soft region 5 is coaligned with CK94's fast shell R139W, which shows blueshifted

emission with velocities up to  $150 \text{ km s}^{-1}$ . The region of bright X-ray emission is  $\sim 15 \text{ pc}$  in diameter and fills a prominent, well-known hole in the H $\alpha$  emission that also appears in the *Spitzer* data (see §8.1). Nearby is another bright, soft X-ray patch (region 6) also  $\sim 15 \text{ pc}$  in diameter that is well-matched to CK94's fast shell R136E. This region exhibits both redshifted and blueshifted emission with speeds in excess of  $130 \text{ km s}^{-1}$ . The X-ray emission is centered on the WR star R145, but CK94 note that it is unlikely to be caused solely by the winds from that one star because the energy requirements to support the X-ray emission and expansion velocities seen would require at least 5 average WR stars. Both X-ray regions 5 and 6 are cooler and intrinsically brighter than their surrounding region 9 (see Figure 8). They may well be parts of the bubble blown by R136 that have been brightened by off-center SNe (Chu & Mac Low 1990).

We find that not every high-velocity feature shows bright X-ray emission. A good example is region 15, which coincides with a 20 pc shell expanding at  $110 \text{ km s}^{-1}$  described by CK94. Figure 8 shows that this region is intrinsically X-ray faint and exhibits the hottest plasma in the 30 Dor nebula. Perhaps this is the site of a recent cavity supernova that occurred far enough from the edge of Shell 2 that it did not produce an X-ray-bright shock but instead deposited its energy into heating the surrounding plasma (Chu & Mac Low 1990). A more detailed velocity study of this region is warranted to elucidate the cause of this unusual X-ray feature.

### 7.2. Is the West Ring a Cavity Supernova Remnant?

A prominent feature in all X-ray images featured in this paper is a nearly-complete, clumpy ring structure in the middle of Shell 3, as described in §4.1. We called this structure the "West Ring" and find that it sits  $\sim 1'$  west of CK94's high-velocity "NW Loop," which shows expansion velocities of  $200 \text{ km s}^{-1}$ . CK94 note that such high velocities are never found in wind-blown bubbles. In Figure 8, the West Ring is contained in region 17, which is indistinguishable from its surrounding region 16 in obscuration and temperature but has slightly higher intrinsic surface brightness.

The West Ring could be a SNR: Meaburn

(1988) performed an echelle study of this region and concluded that the large expansion velocities make a supernova origin the most likely explanation. It resembles the “shell” SNRs catalogued in Williams et al. (1999), both in size and structure. Such a ring structure is predicted by Velázquez et al. (2003) when a SNR hits its cluster’s stellar winds. Recent echelle spectroscopy concentrating on this region also finds knots and shells consistent with a supernova interpretation (Redman et al. 2003).

This structure is also very similar to the central X-ray ring (Leahy et al. 1985) in the over-sized Galactic SNR HB3 (G132.7+1.3), considered to be a cavity SNR (Routledge et al. 1991). The West Ring is about 2'·5 in diameter, or  $\sim 36$  pc. The X-ray ring in HB3 is about 35' in diameter, which at  $D = 2.3$  kpc corresponds to  $\sim 23$  pc. HB3’s X-ray ring is also very clumpy and not quite complete (Landecker et al. 1987); it is strikingly similar in appearance to the West Ring. From Table 3, diffuse region 17 has 0.5–8 keV intrinsic luminosity  $L_{X,corr} = 4.7 \times 10^{35}$  ergs s $^{-1}$  and  $kT = 0.5$  keV. The *Einstein* (0.2–4 keV) X-ray luminosity of HB3 totals  $1.6 \times 10^{35}$  ergs s $^{-1}$  and shows a hot central region ( $kT \sim 1$  keV) evolving to a cooler limb ( $kT \sim 0.3$  keV) (Leahy et al. 1985). Our spectral fit to region 17 shows solar abundances for O and Ne; a recent analysis of a short *XMM* observation of HB3 shows the possibility of enhanced abundances of O, Ne, and Mg in its X-ray ring (Lazendic & Slane 2005). Just as in the West Ring, HB3 lacks strong X-ray emission lines.

Examining the visual and radio images from Dickel et al. (1994), it is clear that there is no prominent visual or radio continuum source at the location of the West Ring. As noted by Chu et al. (2000) in their study of the large LMC X-ray ring RX J050736-6847.8, though, SNRs in low-density media are not expected to show prominent visual or radio features. Given the similarity of the West Ring to HB3 and other LMC SNRs, we suspect that it is in fact a cavity SNR, perhaps produced by a star in the Hodge 301 cluster.

Although more detailed comparisons of the data from CK94 and other kinematic studies to the diffuse X-ray structures revealed by *Chandra* are beyond the scope of this paper, CK94 noted that such comparisons likely hold the key to understanding the complex ISM in 30 Dor. We will

search for the parsec-scale high-velocity knots seen by CK94 and Meaburn (1984) in the longer *Chandra* observation. We suspect that this dataset will reveal small-scale diffuse X-ray features that will merit new kinematic studies as well.

## 8. DISCUSSION

### 8.1. The Relationship between Hot, Warm, and Cool Interstellar Material in 30 Dor

The morphology of the hot X-ray emitting plasma is extremely complicated and bears little resemblance to theoretical calculations of individual SNRs or superbubbles, which generally predict quasi-spherical structures. Insight into the origins of these structures emerges from comparison with the distribution of interstellar material traced by H $\alpha$  emission from ionized gas and IR emission from dust. The comparison with H $\alpha$  has been made since the earliest X-ray images of 30 Dor were obtained by *Einstein* (e.g. Chu & Mac Low 1990; Walborn 1991; Wang & Helfand 1991a).

Figure 12 shows a high-resolution H $\alpha$  image from the MCELS project (C. Smith et al. 2000) in red, with adaptively-smoothed soft-band ACIS images (point sources removed) in green and blue. This image is reminiscent of earlier combinations of H $\alpha$  and X-ray data that showed that diffuse soft X-ray emission was anticorrelated with H $\alpha$  emission, often filling the cavities outlined by ionized gas (e.g. Wang 1999). These high-resolution images allow us to refine that picture somewhat, giving more detailed information on the relative locations of harder and softer X-rays and H $\alpha$  emission.

Comparing Figure 12 to a similar image based on *ROSAT/HRI* data in Wang (1999, Figure 3), both images show that the northern Shell 5 and southern Shell 2 are very clearly outlined by large-scale H $\alpha$  structures. X-rays from the northern part of SNR N157B coincide with a dark cavity in the H $\alpha$  emission caused by a dust lane (Chu et al. 1992). Conversely, the outer loop of Shell 3, labeled as X-ray emitting region 18 in Figure 7, coincides with a similar loop in H $\alpha$ ; in Figure 12 we can see that the northern part of this loop is softer than the southern part. Both images show that a prominent H $\alpha$  dark region in Shell 2 (southeast of R136) contains faint X-ray emission, while the bright H $\alpha$  filaments that outline it bifurcate

our X-ray void labeled region 15. Figure 12 shows that Shell 2 X-rays are relatively hard and Figure 8 reveals that this is due to a combination of intrinsic spectral hardness and heavy obscuration in this part of 30 Dor. The West Ring is now more clearly seen to be a clumpy ring of X-ray emission, fainter in its center, with some soft X-ray emission coincident with the Hodge 301 cluster on the northeast edge of the ring. Small-scale clumps (such as our regions 7 and 8) are now distinct from the smoother underlying X-ray emission. With *Chandra*'s high on-axis spatial resolution, we have been able to excise the point source X-ray emission from Figure 12, so it is clearer that bright diffuse regions 5 and 6 are distinct from the R136 cluster and from the nearby WR stars R139, R140, and R145.

The  $8\mu\text{m}$  *Spitzer* data (Figure 13) highlighting warm dust also add insight into the diffuse X-ray structures. Hot X-ray plasma fills the interiors of superbubbles that are outlined by warm dust and emission from PAHs (Brandl et al. 2006, in preparation). The X-ray morphology and possible confinement are more fully appreciated when anchored by these IR data. Heated dust provides an envelope to the base of the cylindrical X-ray Shell 5. X-ray emission could be suppressed in this region or it could be present but absorbed. An IR-bright V-shaped ridge of emission (reminiscent of the Carina Nebula) separating Shell 3 from Shell 5 is devoid of observable soft X-ray plasma, while the bright X-ray spot dominating Shell 1 is nearly devoid of IR emission. The thermal plasma that constitutes the outer regions of the N157B SNR fills a large cavity in the warm dust. One of the brightest clumps of diffuse X-rays (our region 5) fills a distinct hole in both the  $\text{H}\alpha$  and IR emission.

To give a more complete view of the wide range of emission from 30 Dor, Figure 14 combines the  $8\mu\text{m}$  data tracing PAH emission and warm dust (red) from Figure 13, the  $\text{H}\alpha$  data tracing ionized  $10^4$  K gas (green) from Figure 12, and the 1120–2320 eV X-ray data tracing  $10^7$  K plasma (blue) from Figure 1. Note that here the X-ray image comes from the ACIS data processed with *csmooth*, with the point sources left in place, not the adaptively-smoothed images used in Figures 12 and 13 where the point sources were removed.

Figure 14 shows the full ACIS-I field of view

and is scaled to show the full extent of faint diffuse X-ray emission across the field. The zoomed image in Figure 15 is scaled to show just the brighter patches of X-ray emission in the center of the field and removes the color saturation in the core. Although the *Chandra* data are not deep enough to match the spatial resolution seen in the  $\text{H}\alpha$  and *Spitzer* data, it is clear that the 30 Dor complex cannot be understood by visual and IR studies alone, no matter how high the quality of those datasets. The high-energy emission is a near-perfect complement to the longer-wavelength emission, filling cavities in the complex that are outlined by HII regions. These are in turn outlined by warm dust, because ultraviolet radiation in the HII regions destroys PAHs.

X-rays from the northern parts of SNR N157B fill a prominent hole in the  $8\mu\text{m}$  emission. The eastern side of the Shell 5 X-ray emission, which appeared unconfined by warm dust in Figure 13, is clearly defined by a large region of  $\text{H}\alpha$  emission, while its western side shows a narrower HII region bordered by dust. The southwestern side of the 30 Dor complex shows more warm dust than the northern or eastern sides.

There is a notable absence of X-ray emission in the southeastern corner of the image, where the stellar cluster SL 639 (Shapley & Lindsay 1963; Melnick 1987; Bica et al. 1999) is clearly seen in the  $\text{H}\alpha$  and  $8\mu\text{m}$  data. Some ionized gas is present around the cluster along with substantial amounts of heated dust. This cluster may be too young to have produced a substantial wind-blown bubble or any supernovae, or its ionizing stars may not generate enough wind power to blow a substantial bubble. Conversely, if it is older than  $\sim 10$  Myr it may have dispersed its hot gas. It will be an interesting site to search for faint diffuse X-rays in longer observations.

The famous central arcs north and west of R136 are bright at  $8\mu\text{m}$  as well as in  $\text{H}\alpha$ , illustrating the transition layers from cold molecular material to heated dust to ionized gas that characterize much of the 30 Dor complex. Figure 15 shows that the bright X-ray emission lies in the cavities interior to these ionization fronts, but the saturated center of Figure 14 suggests that some diffuse X-rays are seen superposed on the  $\text{H}\alpha$  and IR emission. This is true in other parts of the image as well and implies that the soft X-rays come from regions that

lie in front of the denser IR-emitting material since they avoided being absorbed. This is a reminder that the complex ISM in 30 Dor may be absorbing similar soft X-rays along other lines of sight. Thus the regions exhibiting hot plasma may be connected via tunnels or fissures that are not visible to us in these images. The regions where we do not see soft X-ray emission are not necessarily lacking in hot plasma, especially if it is clear from the *Spitzer* data that substantial absorbing material lies along the line of sight.

These data thus augment and support the ideas developed over the last twenty years for the evolution of the 30 Dor complex. Powerful stellar winds from extremely massive stars are carving holes in an extensive GMC and filling those holes with hot plasma. Additional hot plasma is added as those stars explode inside the cavities they created. In this process, cold gas is pushed aside and confines the hot plasma into shapes otherwise difficult to understand. Since this plasma appears to emit only soft X-rays for most of its lifetime, some of it may be absorbed by intervening molecular material. Tunnels and fissures could exist in the GMC that allow hot plasma to flow between apparently unconnected regions, although none of the hot plasma seen by *Chandra* appears completely unconfined (there are no empty bubbles that appear to have vented their X-ray plasma into the surrounding ISM). The H $\alpha$  emission traces the ionization fronts, HII region “sheets” that mark the transition between the million-degree plasma and the neutral material. This transition layer is heated, evaporated, and is accelerating away from the cloud interface. Evolved stars are distributed across the entire 30 Dor nebula, providing the fuel for the SNRs that occasionally brighten the superbubbles in X-rays and the enhanced density that allows the plasma to cool. Neutral clumps may also enhance the X-ray emission, especially in regions close to the remains of the GMC.

## 8.2. Summary of Findings

Diffuse emission dominates the morphology of 30 Dor in soft X-rays, caused by hot plasma filling the large superbubbles created by generations of star formation and subsequent SNe in this region. This is dramatically illustrated by combining the *Chandra* data with H $\alpha$  and *Spitzer* images (Figures 12–15); the 10<sup>6</sup>–10<sup>7</sup> K X-ray plasmas are en-

veloped and probably confined in most cases by the cooler gas and warm dust that define the classic picture of 30 Dor. This example illustrates the need for high-quality X-ray observations of star-forming regions; new facets of both stellar and diffuse components are revealed by high-energy data.

The combined spatial and spectral resolution afforded by ACIS shows that these superbubbles are not uniformly filled with a single-temperature gas; great variety is seen, on a range of spatial scales, in absorption, plasma temperature, and intrinsic surface brightness (Figure 8). Some bubbles are center-filled, perhaps revealing interactions with cold gas left in shell interiors (Arthur & Henney 1996; Wang 1999), while others are edge-brightened with distinct central voids not caused by obscuring foreground material. The faintest regions (voids and the periphery of the main 30 Dor nebula) are a factor of 20 fainter in intrinsic surface brightness than the brightest regions, which have surface brightnesses  $> 1 \times 10^{33}$  ergs s<sup>-1</sup> pc<sup>-2</sup>. Our diffuse regions range in size from 1' ( $\sim 14.5$  pc) for small surface brightness enhancements to  $> 7'$  for the large shells. For comparison with other GEHRs, we have provided integrated spectra and fits for the main 30 Dor nebula and for the N157B SNR (Table 2).

Spectral fits to the diffuse emission show moderate absorption ( $N_H = 1\text{--}6 \times 10^{21}$  cm<sup>-2</sup>) and soft thermal plasmas with  $kT = 0.3\text{--}0.8$  keV (3–9 MK). Many diffuse regions exhibit elevated abundances (above the nominal value of 0.3Z<sub>⊙</sub>), perhaps indicative of line emission, but none show prominent emission lines. Although not a definitive demonstration of a supernova origin for the X-ray emission, these spectral fit results are consistent with that interpretation. SNR N157B, also possibly the result of an explosion within a pre-existing cavity, also lacks strong emission lines, as does the Galactic example of a possible cavity SNR discussed here, HB3.

The brightest point source in the field is PSR J0537–6910 in the SNR N157B, imaged almost 7' off-axis. Although the large PSF there prevents us from performing accurate spectral analysis of the pulsar and its pulsar wind nebula, these data clearly show spectral changes as a function of distance from the pulsar; the pure non-thermal spectrum steepens and combines with a thermal component, finally giving over to a pure

thermal spectrum in the outer regions of the SNR (§6).

Several interesting smaller-scale structures emerge with the high-resolution *Chandra* observations. One feature (the “West Ring”) may be the relic signature of a past cavity supernova that exploded inside a pre-existing wind-blown bubble generated by the Hodge 301 cluster. As first shown by CK94, bright patches of X-ray emission often coincide with high-velocity features known from H $\alpha$  echelle studies, indicating that X-rays are produced in shocks in 30 Dor’s ISM (§7).

The MCELS H $\alpha$  image, the *Spitzer* image, and the recent mosaic of *HST* data (Walborn et al. 2002) are all dominated by highly-structured arcs and shells on 1–10 pc scales; in the central region, these reveal the interfaces between the central cavity created by R136 and the surrounding molecular clouds (Scowen et al. 1998) and demonstrate how R136 is shredding its natal environment (§8.1). Here and throughout the 30 Dor nebula, an appreciation of the X-ray emission is necessary to further our understanding of the processes working to shape this complex. As the images in §8.1 show, it is imperative that the diffuse X-ray emission become part of the “classic” picture of 30 Dor.

New stellar clusters are now forming in the dense knots that remain in 30 Dor’s GMC; their collapse was probably triggered by R136 (Walborn et al. 2002). These clusters are not yet resolved in X-rays, demonstrating that there is much more work to be done to achieve a complete picture of the X-ray emission from 30 Dor.

### 8.3. 30 Dor and Other Massive Star-forming Regions

30 Dor’s diffuse X-ray emission is, overall, substantially different than that seen in Galactic MS-FRs that are too young to have produced SNe. M 17 shows strong diffuse soft X-rays probably due to wind-wind and/or wind-cloud collisions (Townsley et al. 2003), but the primary component of this emission is hotter ( $kT = 0.6$  keV) than many 30 Dor regions and has low surface brightness ( $10^{31.9}$  ergs s $^{-1}$  pc $^{-2}$ ). These quantities are most similar to the regions we call “voids” in 30 Dor (regions 15, 19, 20, 21, and 22 in Figure 7). The diffuse X-ray emission reported for the massive Galactic clusters NGC 3603 (Mof-

fat et al. 2002) and Arches (Yusef-Zadeh et al. 2002) has higher surface brightness more comparable to the brighter regions in 30 Dor ( $10^{32.6}$  and  $10^{33.1}$  ergs s $^{-1}$  pc $^{-2}$  respectively, calculated from Table 4 of Townsley et al. 2003) but the plasmas are much hotter ( $kT = 3.1$  keV and 5.7 keV respectively). Either a very different mechanism is generating hard diffuse emission in these clusters (e.g. wind collisions, Cantó, Raga, & Rodríguez 2000), young SNe dominate the diffuse emission, or substantial unresolved point source emission is corrupting the measurements.

Chu et al. (1993) proposed that the soft diffuse X-ray emission seen in the Carina star-forming complex (Seward & Chlebowski 1982) could be due to a cavity SNR inside a superbubble blown by Carina’s many massive stellar clusters; thus the Carina complex should be a Galactic analog to one of the superbubbles seen in 30 Dor. The entire Carina complex shows integrated X-ray emission with  $kT \sim 0.8$  keV and surface brightness  $\geq 10^{32.2}$  ergs s $^{-1}$  pc $^{-2}$  (Seward & Chlebowski 1982; Townsley et al. 2003). *Chandra* and *XMM* resolve this X-ray emission into thousands of harder but comparatively faint stellar sources (e.g. Albacete Colombo et al. 2003; Evans et al. 2003) and bright diffuse emission pervading the complex yet not centered on the O or WR stars or the stellar clusters. No obvious SNR is present, but the complex is old enough to have produced SNe, as evidenced by the presence of evolved stars. This bright, soft diffuse emission is quite comparable in surface brightness and extent to the smaller regions sampled in 30 Dor. Using new *Chandra* data centered on the Trumpler 14 OB cluster in Carina, we show that the brightest regions of diffuse emission are well-separated from the massive stars in the Carina complex and show filamentary morphology, both consistent with a cavity supernova origin (Townsley et al. 2005a). Thus we suspect that Carina serves as a good microscope for understanding the processes powering the X-ray emission from 30 Dor.

Given the morphological complexity that 30 Dor displays at all wavelengths, it is surprisingly similar to other GEHRs, most notably NGC 604 in M33, the second-largest GEHR in the Local Group. Although not dominated by a massive central star cluster, the large-scale loops and voids of NGC 604 are also characteristic of superbubbles

and are filled with hot gas emitting soft X-rays (Maíz-Apellániz et al. 2004, Brandl et al. 2006, in preparation). The second-largest GEHR in the LMC, N11, also exhibits a central massive stellar cluster surrounded by a superbubble and containing bright, soft diffuse X-rays (Mac Low et al. 1998; Nazé et al. 2004). Although more distant GEHRs are not resolvable with current technology, we should expect all GEHRs to be made up of a complex mix of pointlike and diffuse X-ray components with the hard-band X-ray luminosity dominated by massive stars and the soft-band X-ray luminosity dominated by the effects of recent cavity SNe exploding near the edges of superbubbles, as we see in 30 Dor.

#### 8.4. Concluding Comments

We have analyzed an early *Chandra*/ACIS observation of 30 Doradus, concentrating here on the diffuse X-ray structures and in Paper II on the point sources. This study documents a wide variety of diffuse X-ray-emitting sources: a complex hierarchy of diffuse structures, from small-scale knots and wisps to huge superbubbles; a composite SNR including its pulsar, pulsar wind nebula, and cometary tail; an X-ray ring possibly due to a cavity SNR; bright X-ray patches associated with high-velocity H $\alpha$  structures. A coherent understanding of the structures is beginning to emerge from a multiwavelength comparison of the X-ray, H $\alpha$ , and mid-IR maps. We demonstrate a variety of data analysis tools for study of ACIS fields with mixtures of pointlike sources and diffuse structures. All software used in this study is publicly available.

From this work, we conclude the following:

- 30 Dor's integrated diffuse emission is well-fit by a single-temperature plasma with  $T \simeq 7$  MK, roughly solar line strengths, and a single absorbing column density of  $N_H \simeq 3 \times 10^{21}$  cm $^{-2}$ . The soft-band luminosity is dominated by the diffuse structures, but these disappear above 2 keV and the integrated emission is dominated by just a few bright point sources (§4.3 and Paper II).
- ACIS spectra of 30 Dor's diffuse emission regions often suggest chemical enrichment, another argument in favor of a SNR origin for the X-ray emission (Table 3).
- Annular spectra around the SNR N157B, centered on PSR J0537–6910, indicate electron cooling through a steepening power law slope, a transition from non-thermal to thermal spectra with distance from the pulsar, and chemical enrichment in the SNR (§6).
- A powerful method for understanding the complex spectral and spatial information contained in high-resolution X-ray studies of massive star-forming complexes like 30 Dor is to study maps of column density, plasma temperature, and intrinsic surface brightness derived from X-ray spectral fitting (Figure 8).
- The main 30 Dor nebula exhibits several X-ray “voids” not caused by obscuration, most notably the hot region 15 (§5.2). These resemble the wind collision plasma seen in nearby HII regions like M 17 (§8.3).
- Comparing the diffuse X-ray emission with kinematic studies of the warm gas in HII region complexes is essential to disentangle the confusing morphological information. While the fast shocks found in 30 Dor by CK94 often correlate well with regions of high X-ray surface brightness, the correlation is not complete; some fast shells lack bright X-rays while some X-ray features are not known to exhibit high velocities (§7.1).
- Some shells do not currently contain massive clusters to supply wind-generated X-rays. The source of diffuse X-rays may be centered SNe that heated the interior of these shells without producing fast shocks against the shell walls (Chu & Mac Low 1990).
- The X-ray structure that we call the West Ring (our region 17) is adjacent to CK94's NW Loop and has X-ray properties very similar to the Galactic cavity SNR HB3. We propose that it is a cavity SNR that exploded inside 30 Dor's Shell 3 and that its progenitor most likely came from the massive cluster Hodge 301 (§7.2).
- Bright X-ray patches often have cooler plasma temperatures than their surrounding shells, possibly indicating that the increased densities associated with fast shocks allow

the associated X-ray plasma to cool more efficiently than the plasma associated with the large, low-density shells.

Our upcoming 100 ks ACIS-I observation of 30 Dor will provide the high-quality X-ray dataset that is needed to place the X-ray emission in context with state-of-the-art observations in other wavebands. We expect this observation to reveal more of the high-mass stellar population in 30 Dor and to give even more detailed information on the complex morphology of the wind-blown bubbles and superbubbles, both with higher spatial resolution imaging and with spectroscopy on finer spatial scales. True progress in understanding, though, will require cooperation. By combining the power of today's Great Observatories and high-quality ground-based data, we are confident that unique insight awaits.

Support for this work was provided to Gordon Garmire, the ACIS Principal Investigator, by the National Aeronautics and Space Administration (NASA) through NASA Contract NAS8-38252 and *Chandra* Contract SV4-74018 issued by the *Chandra X-ray Observatory* Center, which is operated by the Smithsonian Astrophysical Observatory for and on behalf of NASA under contract NAS8-03060. LKT appreciates technical contributions by Jeremy Sanders and Konstantin Getman and helpful discussions with Mike Eracleous and Bruce Elmegreen. We thank the Magellanic Cloud Emission Line Survey (MCELS) team for the use of their H $\alpha$  image of 30 Doradus. We also thank our anonymous referee for investing the time to review this paper and for several helpful suggestions.

This work is based in part on observations made with the *Spitzer Space Telescope*, which is operated by the Jet Propulsion Laboratory, California Institute of Technology under NASA Contract 1407. This research made use of data products from the Two Micron All Sky Survey, which is a joint project of the University of Massachusetts and the Infrared Processing and Analysis Center/California Institute of Technology, funded by NASA and the National Science Foundation. This research also made use of the SIMBAD database and VizieR catalogue access tool, operated at CDS, Strasbourg, France. We are grateful for the

invaluable tools of NASA's Astrophysics Data System.

## REFERENCES

- Albacete Colombo, J. F., Méndez, M., & Morrell, N. I. 2003, MNRAS, 346, 704
- Arnaud, K. A. 1996, in ASP Conf. Ser. 101, Astronomical Data Analysis Software and Systems V, ed. G. H. Jacoby & J. Barnes (San Francisco: ASP), 17
- Arthur, S. J., & Henney, W. J. 1996, ApJ, 457, 752
- Bamba, A., Ueno, M., Nakajima, H., & Koyama, K. 2004, ApJ, 602, 257
- Behar, E., Rasmussen, A. P., Griffiths, R. G., Dennerl, K., Audard, M., Aschenbach, B., & Brinkman, A. C. 2001, A&A, 365, L242
- Bica, E. L. D., Schmitt, H. R., Dutra, C. M., & Oliveira, H. L. 1999, AJ, 117, 238
- Brandl, B. R. 2005, in ASSL Vol. 329, Starbursts: From 30 Doradus to Lyman Break Galaxies, ed. R. de Grijs & R. M. González Delgado (Dordrecht: Springer), 49
- Broos, P., et al. 2000, User's Guide for the TARA Package (University Park: Pennsylvania State Univ.)
- Broos, P. S., Townsley, L. K., Getman, K. V., & Bauer, F. E. 2002, ACIS Extract, An ACIS Point Source Extraction Package (University Park: Pennsylvania State Univ.)
- Cantó, J., Raga, A. C., & Rodríguez, L. F. 2000, ApJ, 536, 896
- Chen, C.-H. R., Chu, Y., & Johnson, K. E. 2005, ApJ, 619, 779
- Chu, Y. & Mac Low, M. 1990, ApJ, 365, 510
- Chu, Y., Kennicutt, R. C., Schommer, R. A., & Laff, J. 1992, AJ, 103, 1545
- Chu, Y., Low, M. M., Garcia-Segura, G., Wakker, B., & Kennicutt, R. C. 1993, ApJ, 414, 213
- Chu, Y., & Kennicutt, R. C. 1994, ApJ, 425, 720
- Chu, Y., Chang, H., Su, Y., & Mac Low, M. 1995a, ApJ, 450, 157
- Chu, Y., Dickel, J. R., Staveley-Smith, L., Osterberg, J., & Smith, R. C. 1995b, AJ, 109, 1729
- Chu, Y., Kim, S., Points, S. D., Petre, R., & Snowden, S. L. 2000, AJ, 119, 2242
- Chu, Y., Gruendl, R. A., Chen, C.-H. R., Lazendic, J. S., & Dickel, J. R. 2004, ApJ, 615, 727
- Clark, D. H., Tuohy, I. R., Dopita, M. A., Mathewson, D. S., Long, K. S., Szymkowiak, A. E., & Culhane, J. L. 1982, ApJ, 255, 440
- Crawford, F., McLaughlin, M., Johnston, S., Romani, R., & Sorrelgreen, E. 2005, in 35th COSPAR Scientific Assembly, 854
- Cusumano, G., Maccarone, M. C., Mineo, T., Sacco, B., Massaro, E., Bandiera, R., & Salvati, M. 1998, A&A, 333, L55
- Dennerl, K. et al. 2001, A&A, 365, L202
- Dickel, J. R., Milne, D. K., Kennicutt, R. C., Chu, Y., & Schommer, R. A. 1994, AJ, 107, 1067
- Dunne, B. C., Points, S. D., & Chu, Y. 2001, ApJS, 136, 119
- Evans, N. R., Seward, F. D., Krauss, M. I., Isobe, T., Nichols, J., Schlegel, E. M., & Wolk, S. J. 2003, ApJ, 589, 509
- Feast, M. W., Thackeray, A. D., & Wesselink, A. J. 1960, MNRAS, 121, 337
- Freeman, P. E., Kashyap, V., Rosner, R., & Lamb, D. Q. 2002, ApJS, 138, 185
- Getman, K. V., et al. 2005, ApJS, 160, 319
- Grebel, E. K., & Chu, Y. 2000, AJ, 119, 787
- Haberl, F., & Pietsch, W. 1999, A&AS, 139, 277
- Haberl, F., Dennerl, K., Filipović, M. D., Aschenbach, B., Pietsch, W., & Trümper, J. 2001, A&A, 365, L208
- Higdon, J. C., Lingenfelter, R. E., & Ramaty, R. 1998, ApJ, 509, L33
- Johansson, L. E. B., et al. 1998, A&A, 331, 857
- Landecker, T. L., Dewdney, P. E., Vaneldik, J. F., & Routledge, D. 1987, AJ, 94, 111

- Lazendic, J. S., Dickel, J. R., & Jones, P. A. 2003, *ApJ*, 596, 287
- Lazendic, J., & Slane, P. 2005, *ApJ*, submitted (astro-ph/0505498)
- Leahy, D. A., Venkatesan, D., Long, K. S., & Naranan, S. 1985, *ApJ*, 294, 183
- Long, K. S., & Helfand, D. J. 1979, *ApJ*, 234, L77
- Long, K. S., Helfand, D. J., & Grabelsky, D. A. 1981, *ApJ*, 248, 925
- Mac Low, M., Chang, T. H., Chu, Y., Points, S. D., Smith, R. C., & Wakker, B. P. 1998, *ApJ*, 493, 260
- Maíz-Apellániz, J., Pérez, E., & Mas-Hesse, J. M. 2004, *AJ*, 128, 1196
- Mark, H., Price, R., Rodrigues, R., Seward, F. D., & Swift, C. D. 1969, *ApJ*, 155, L143
- Marshall, F. E., Gotthelf, E. V., Zhang, W., Mid-dleditch, J., & Wang, Q. D. 1998, *ApJ*, 499, L179
- Meaburn, J. 1984, *MNRAS*, 211, 521
- Meaburn, J. 1988, *MNRAS*, 235, 375
- Melnick, J. 1987, in IAU Symp. 121, Observational Evidence of Activity in Galaxies, ed. E. E. Khachikian, K. J. Fricke & J. Melnick (Dordrecht: Kluwer), 545
- Meurer, G. R., Heckman, T. M., Leitherer, C., Kinney, A., Robert, C., & Garnett, D. R. 1995, *AJ*, 110, 2665
- Mignani, R. P., Pulone, L., Iannicola, G., Pavlov, G. G., Townsley, L., & Kargaltsev, O. Y. 2005, *A&A*, 431, 659
- Moffat, A. F. J. et al. 2002, *ApJ*, 573, 191
- Mori, K., Tsunemi, H., Miyata, E., Baluta, C. J., Burrows, D. N., Garmire, G. P., & Chartas, G. 2001, in ASP Conf. Ser. 251, New Century of X-ray Astronomy, ed. H. Inoue & H. Kunieda (San Francisco: ASP), 576
- Morrison, R. & McCammon, D. 1983, *ApJ*, 270, 119
- Nazé, Y., Hartwell, J. M., Stevens, I. R., Corcoran, M. F., Chu, Y.-H., Koenigsberger, G., Moffat, A. F. J., & Niemela, V. S. 2002, *ApJ*, 580, 225
- Nazé, Y., Antokhin, I. I., Rauw, G., Chu, Y.-H., Gosset, E., & Vreux, J.-M. 2004, *A&A*, 418, 841
- Norci, L., & Ögelman, H. 1995, *A&A*, 302, 879
- Parizot, E., Marcowith, A., van der Swaluw, E., Bykov, A. M., & Tatischeff, V. 2004, *A&A*, 424, 747
- Park, S., Zhekov, S. A., Burrows, D. N., Garmire, G. P., & McCray, D. 2005, Advances in Space Research, 35, 991
- Points, S. D., Chu, Y.-H., Snowden, S. L., & Smith, R. C. 2001, *ApJS*, 136, 99
- Portegies Zwart, S. F., Pooley, D., & Lewin, W. H. G. 2002, *ApJ*, 574, 762
- Redman, M. P., Al-Mostafa, Z. A., Meaburn, J., Bryce, M., & Dyson, J. E. 1999, *A&A*, 345, 943
- Redman, M. P., Al-Mostafa, Z. A., Meaburn, J., & Bryce, M. 2003, *MNRAS*, 344, 741
- Routledge, D., Dewdney, P. E., Landecker, T. L., & Vaneldik, J. F. 1991, *A&A*, 247, 529
- Sanders, J. S., Fabian, A. C., & Taylor, G. B. 2005, *MNRAS*, 356, 1022
- Sasaki, M., Haberl, F., & Pietsch, W. 2000, *A&AS*, 143, 391
- Sasaki, M., Haberl, F., & Pietsch, W. 2002, *A&A*, 392, 103
- Scowen, P. A., et al. 1998, *AJ*, 116, 163
- Seward, F. D. & Chlebowski, T. 1982, *ApJ*, 256, 530
- Shapley, H., & Lindsay, E. M. 1963, *Irish Astron. J.*, 6, 74
- Smith, B. J., Struck, C., & Nowak, M. A. 2005, *AJ*, 129, 1350
- Smith, C., Leiton, R., & Pizarro, S. 2000, in ASP Conf. Ser. 221, Stars, Gas and Dust in Galaxies: Exploring the Links, ed. D. Alloin, K. Olsen, & G. Galaz (San Francisco: ASP), 83

- Smith, D. A., & Wang, Q. D. 2004, ApJ, 611, 881
- Smith, R. K., Brickhouse, N. S., Liedahl, D. A., & Raymond, J. C. 2001, ApJ, 556, L91
- Snowden, S. L., & Petre, R. 1994, ApJ, 436, L123
- Stevens, I. R., & Hartwell, J. M. 2003, MNRAS, 339, 280
- Strickland, D. K., Heckman, T. M., Weaver, K. A., Hoopes, C. G., & Dahlem, M. 2002, ApJ, 568, 689
- Townsley, L., Feigelson, E., Burrows, D., Chu, Y.-H., Garmire, G., Broos, P., Tsuboi, Y., & Griffiths, R. 1999, BAAS, 31, 1453
- Townsley, L. K., Broos, P. S., Garmire, G. P., & Nousek, J. A. 2000, ApJ, 534, L139
- Townsley, L., et al. 2000, BAAS, 32, 1594
- Townsley, L., et al. 2002, APS Meeting Abstracts, 17061
- Townsley, L. K., Broos, P. S., Nousek, J. A., & Garmire, G. P. 2002, Nuclear Instr. & Methods, 486, 751
- Townsley, L. K., Broos, P. S., Chartas, G., Moskalenko, E., Nousek, J. A., & Pavlov, G. G. 2002, Nuclear Instr. & Methods, 486, 716
- Townsley, L. K., Feigelson, E. D., Montmerle, T., Broos, P. S., Chu, Y., & Garmire, G. P. 2003, ApJ, 593, 874
- Townsley, L. K., Broos, P. S., Feigelson, E. D., & Garmire, G. P. 2005, in IAU Symp. 227, Massive Star Birth – A Crossroads of Astrophysics, ed. R. Cesaroni, E. Churchwell, M. Felli, & C. M. Walmsley (astro-ph/0506418)
- Townsley, L. K., Broos, P. S., Feigelson, E. D., Garmire, G. P., & Getman, K. V. 2005, AJ, submitted
- Tsunemi, H., Mori, K., Miyata, E., Baluta, C., Burrows, D. N., Garmire, G. P., & Chartas, G. 2001, ApJ, 554, 496
- Velázquez, P. F., Königsberger, G., & Raga, A. C. 2003, ApJ, 584, 284
- Walborn, N. R. 1991, in IAU Symp. 148, The Magellanic Clouds, ed. R. Haynes & D. Milne (Dordrecht: Kluwer), 145
- Walborn, N. R., Maíz-Apellániz, J., & Barbá, R. H. 2002, AJ, 124, 1601
- Wang, Q., Hamilton, T., Helfand, D. J., & Wu, X. 1991, ApJ, 374, 475
- Wang, Q., & Helfand, D. J. 1991a, ApJ, 370, 541
- Wang, Q., & Helfand, D. J. 1991b, ApJ, 373, 497
- Wang, Q. D. 1995, ApJ, 453, 783
- Wang, Q. D., & Gotthelf, E. V. 1998, ApJ, 494, 623
- Wang, Q. D., & Gotthelf, E. V. 1998, ApJ, 509, L109
- Wang, Q. D. 1999, ApJ, 510, L139
- Wang, Q. D., Gotthelf, E. V., Chu, Y.-H., & Dickel, J. R. 2001, ApJ, 559, 275
- Williams, R. M., Chu, Y., Dickel, J. R., Petre, R., Smith, R. C., & Tavarez, M. 1999, ApJS, 123, 467
- Yusef-Zadeh, F., Law, C., Wardle, M., Wang, Q. D., Fruscione, A., Lang, C. C., & Cotera, A. 2002, ApJ, 570, 665

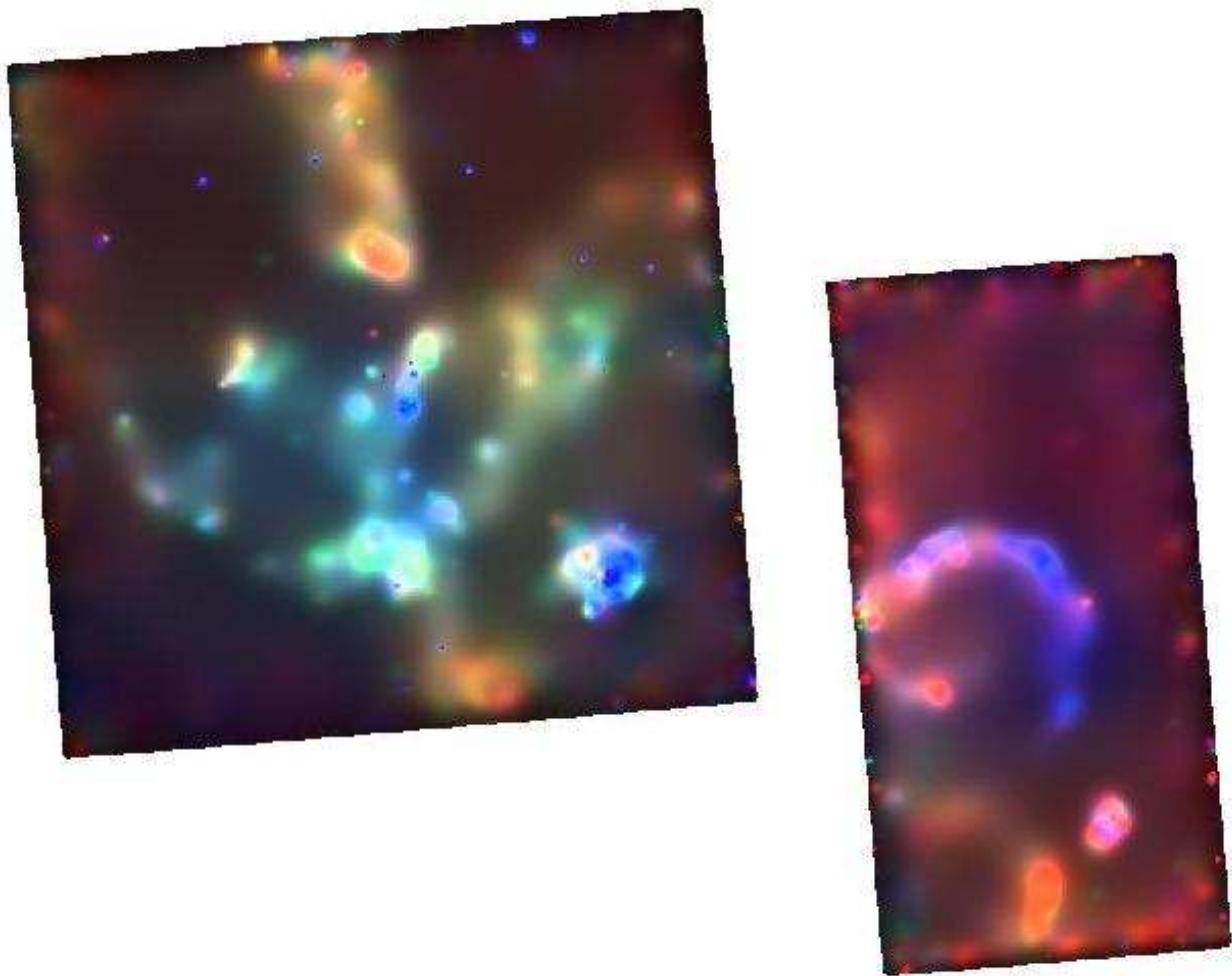


Fig. 1.— An adaptively smoothed image of our *Chandra*/ACIS observation of 30 Doradus, centered on the massive stellar cluster R136 and partially covering a  $\sim 24' \times 30'$  region (roughly 350 pc  $\times$  430 pc at an assumed distance of  $D = 50$  kpc). This rendering emphasizes soft diffuse structures; red = 500–700 eV, green = 700–1120 eV, blue = 1120–2320 eV.

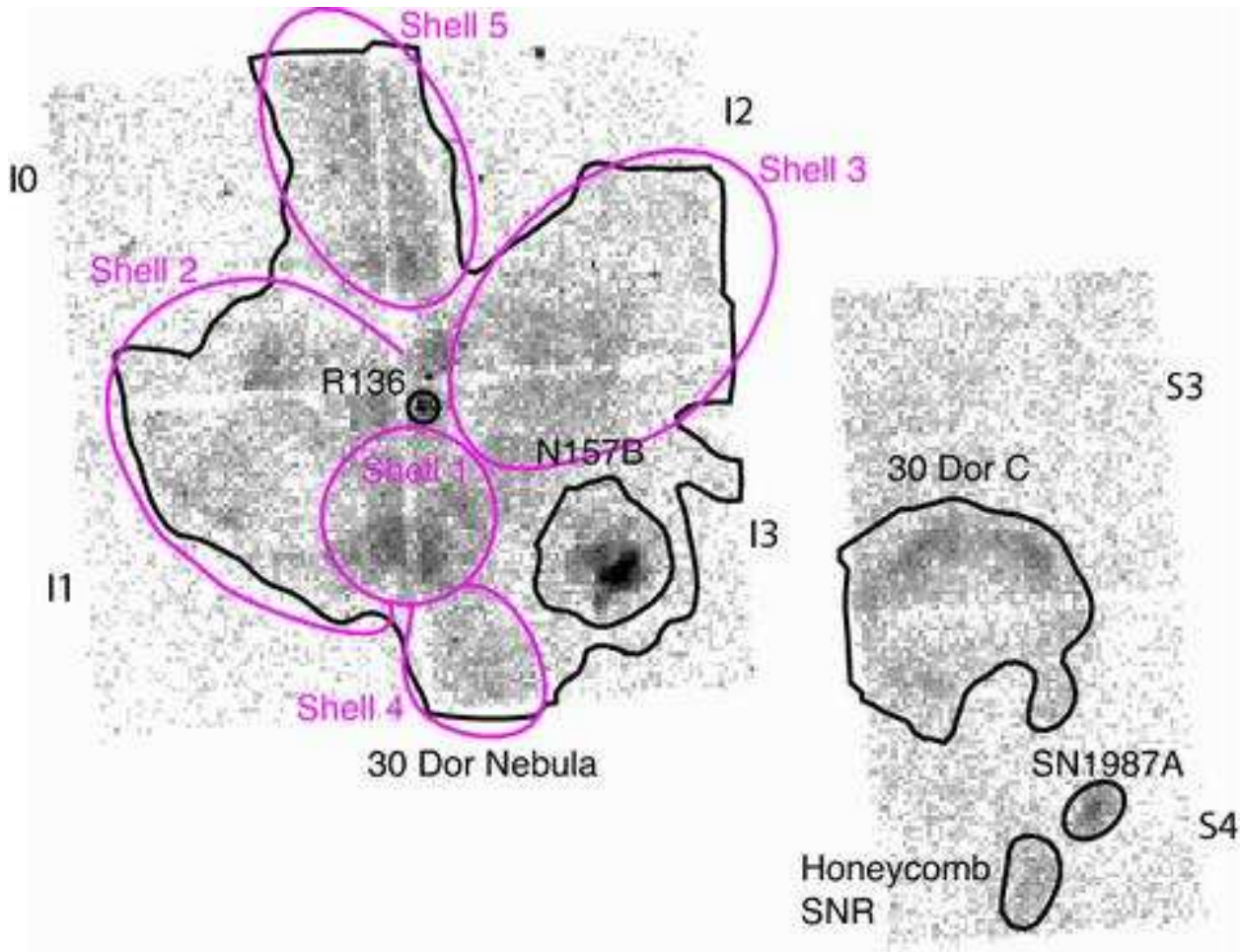


Fig. 2.— 30 Doradus in X-rays, from the 21,870-sec GTO1 *Chandra*/ACIS observation (binned to  $16 \times 16$  ACIS pixels or  $8'' \times 8''$ ), with the ACIS-I array centered on the massive stellar cluster R136. Other well-known structures in the field are labeled; the “shells” are the superbubbles sketched in Wang & Helfand (1991a) and Chu & Kennicutt (1994) based on an H $\alpha$  image from Meaburn (1984). The names of the six ACIS CCDs used in this observation are shown; each CCD covers  $\sim 8''.5 \times 8''.5$ , or  $\sim 120$  pc  $\times$  120 pc at  $D = 50$  kpc.

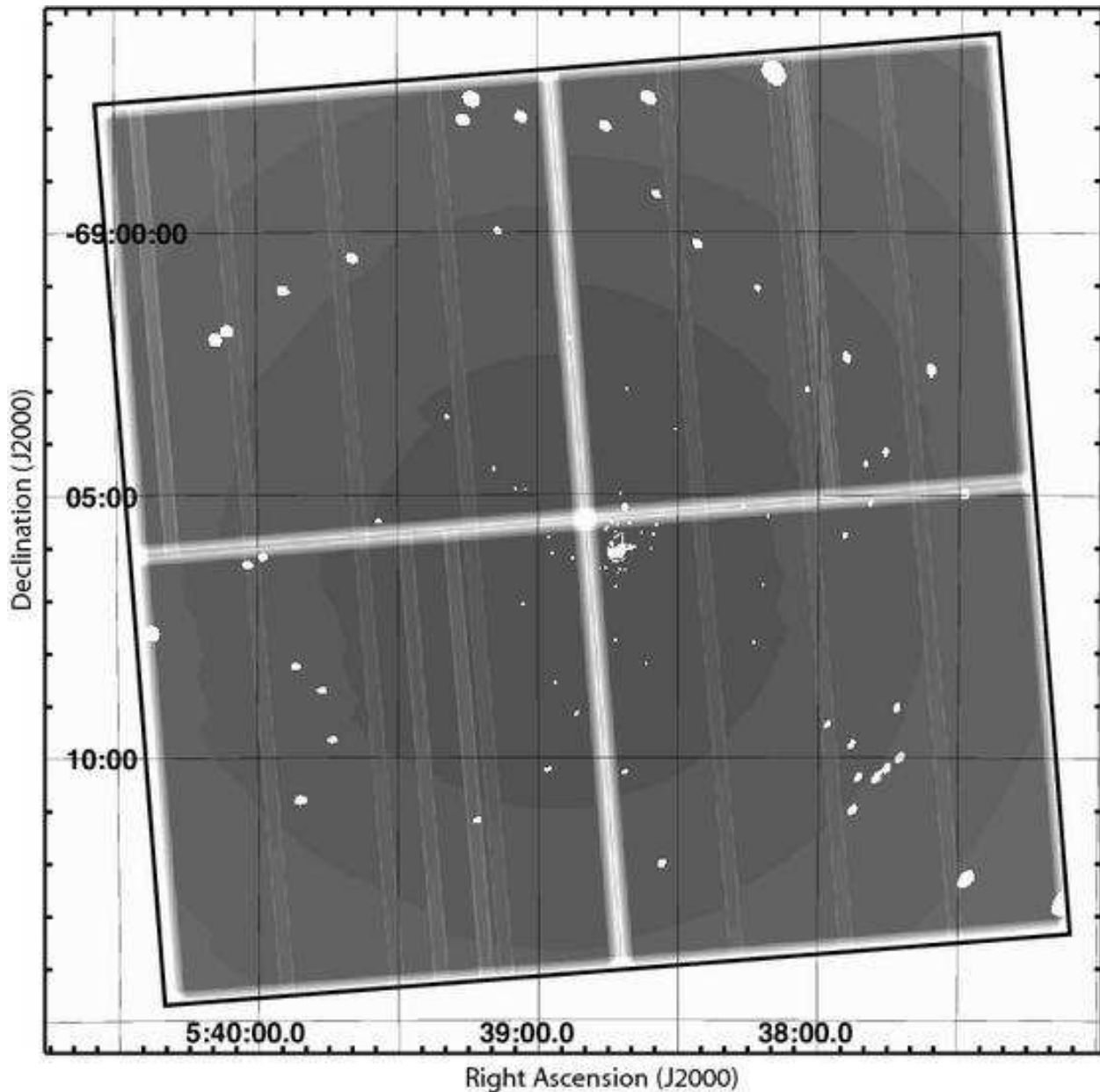


Fig. 3.— The exposure map for ObsID 62520 with point source masks applied, displayed with log scaling (darker areas have higher exposure). Gaps between the four ACIS-I CCDs and bad columns are seen as areas of reduced exposure, while areas of zero exposure due to point source masks are seen as white patches scattered across the field.

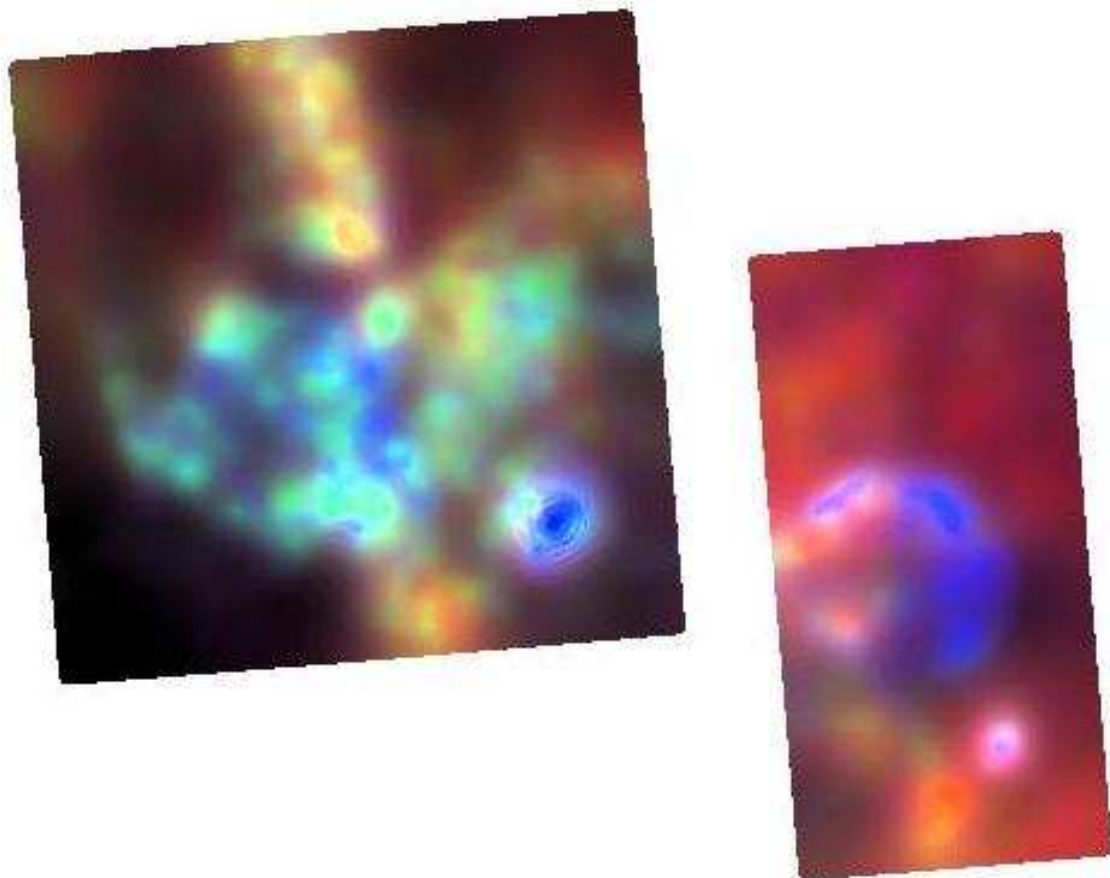


Fig. 4.— 30 Doradus diffuse structures: red = 350–700 eV, green = 700–1100 eV, blue = 1100–2200 eV. This adaptively-smoothed image was generated after 180 point sources were removed from the data and uses a different smoothing tool than Figure 1, for comparison.

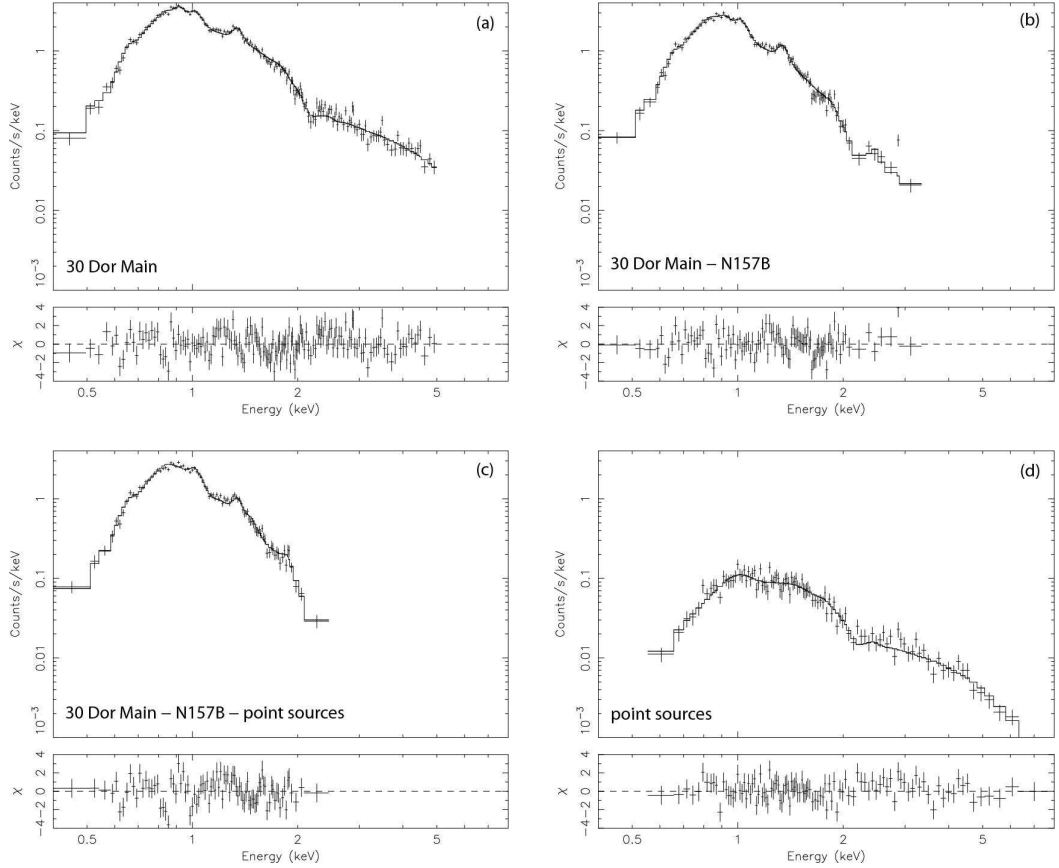


Fig. 5.— Global spectra of the X-ray emission in 30 Dor. For these and all later spectral fits, the upper panels show the instrumental spectra and best-fit models from *XSPEC* while the lower panels show the residuals. The fit parameters are given in Table 2. (a) The composite spectrum of the entire 30 Dor main nebula on the ACIS-I array (as outlined in Figure 2), including all point sources and the SNR N157B. (b) The spectrum of the same region, including point sources but excluding N157B (region shown in Figure 2) and the point sources associated with it. (c) The spectrum of the superbubbles alone; this uses the same extraction region as (b) but the point sources it encloses have been removed. (d) The composite spectrum of the point sources that were removed in (c).

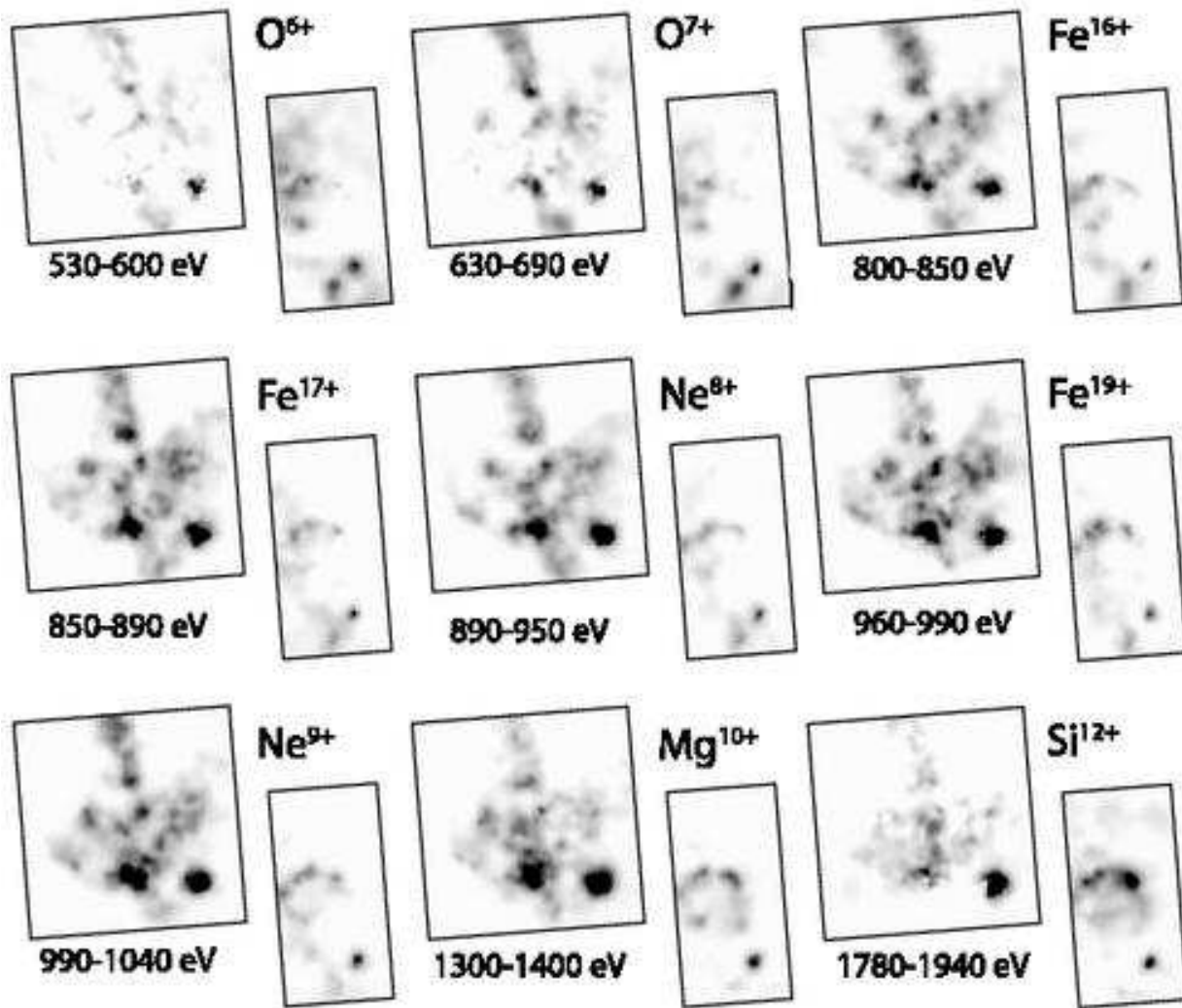


Fig. 6.— Narrow-band smoothed images of the 30 Dor complex in energies corresponding to ions commonly seen in SNRs:  $O^{6+}$  (530–600 eV),  $O^{7+}$  (630–690 eV),  $Fe^{16+}$  (800–850 eV),  $Fe^{17+}$  (850–890 eV),  $Ne^{8+}$  (890–950 eV),  $Fe^{19+}$  (960–990 eV),  $Ne^{9+}$  (990–1040 eV),  $Mg^{10+}$  (1300–1400 eV), and  $Si^{12+}$  (1780–1940 eV).

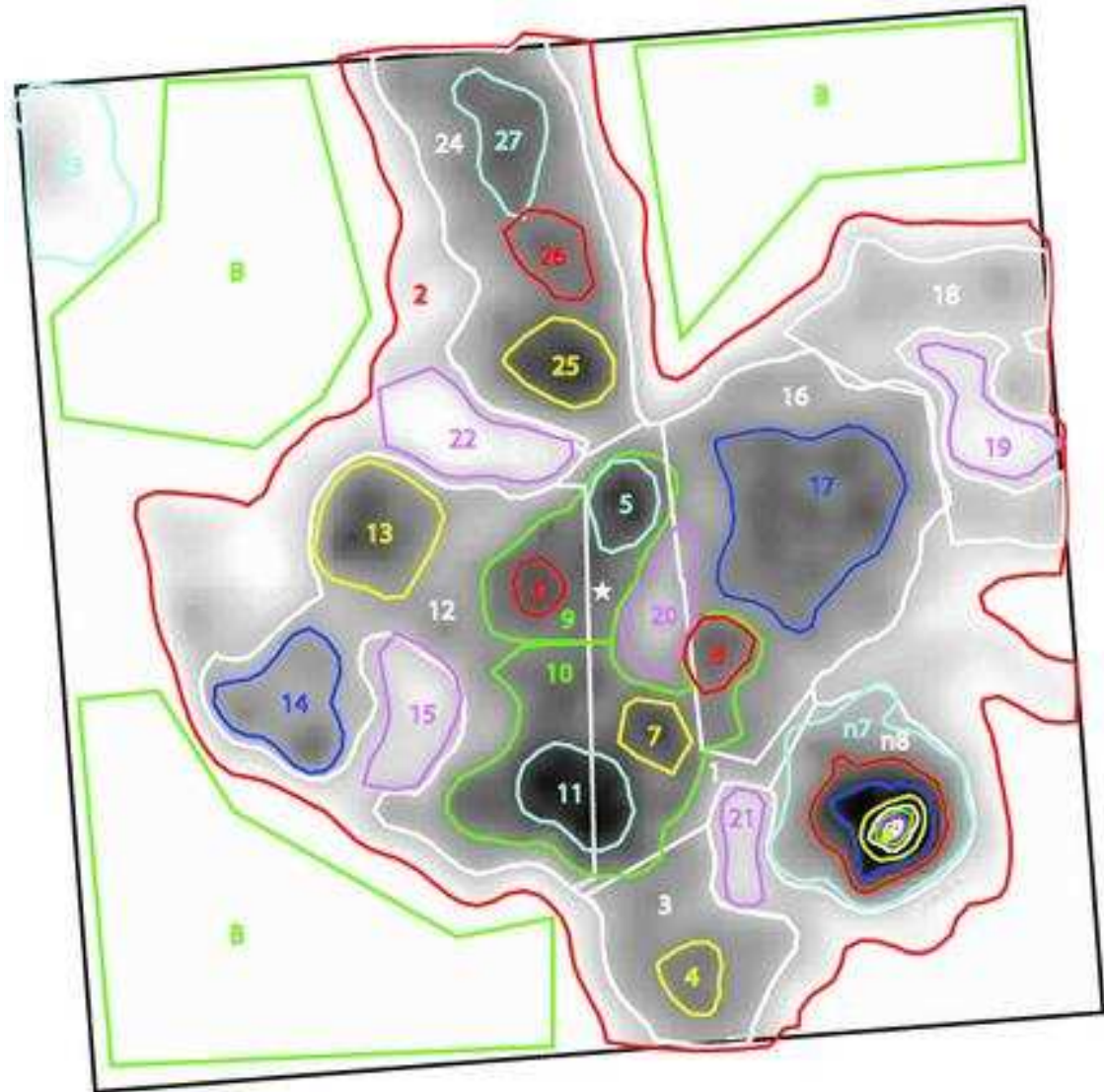


Fig. 7.— Spectral extraction regions for diffuse structures in 30 Dor, overlaid on an adaptively smoothed broadband (350–2000 eV) image of the *Chandra* ACIS-I data, where point sources have been removed to study the diffuse spectra. The small white star in the middle of the figure shows the approximate location of the R136 cluster.

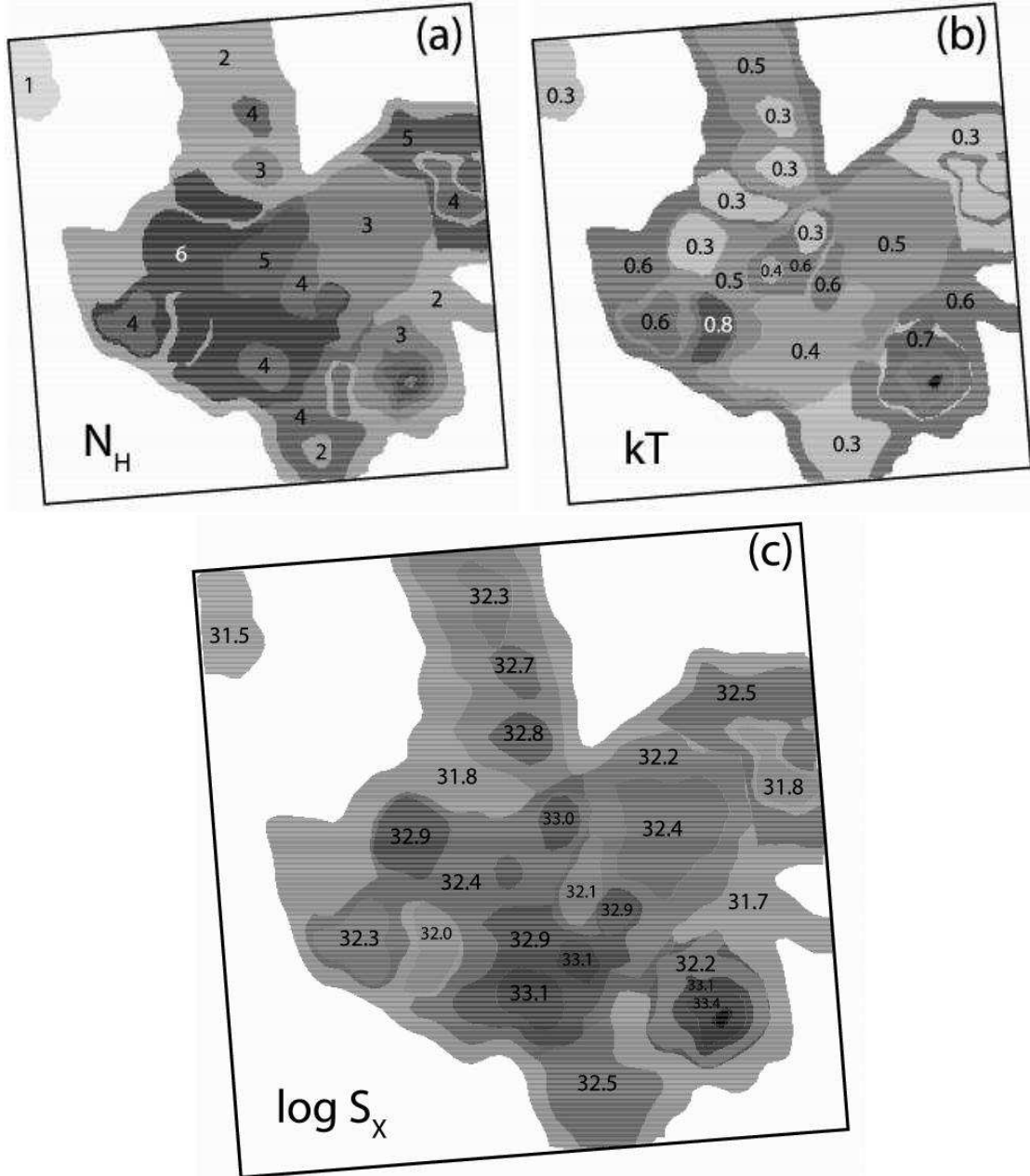


Fig. 8.— Maps of spectral fit parameters for diffuse regions defined in Figure 7. (a) Absorption  $N_H$  in units of  $10^{21} \text{ cm}^{-2}$ . (b) Plasma temperature expressed as  $kT$  (keV). (c) Log of the absorption-corrected soft-band (0.5–2 keV) surface brightness  $S_X$  in units of  $\text{ergs s}^{-1} \text{ pc}^{-2}$ . Spectral fits for each diffuse region consisted of a single absorbed thermal plasma with variable abundances. Apparent “rings” around voids are an artifact of the map-making; see §5.2 for details.

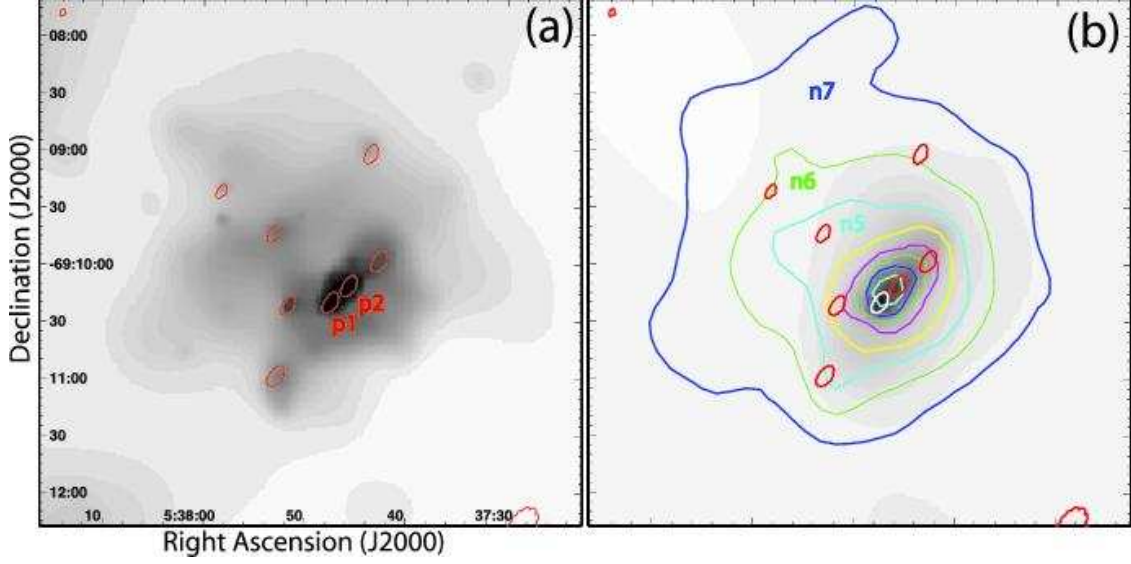


Fig. 9.— The SNR N157B. (a) Soft-band *csmooth* image with pointlike sources shown in red using polygons that define their 90% PSF extraction regions. (b) Diffuse spectral extraction regions (based on full-band smoothed images) overlaid on a hard-band *csmooth* image, same size as (a).

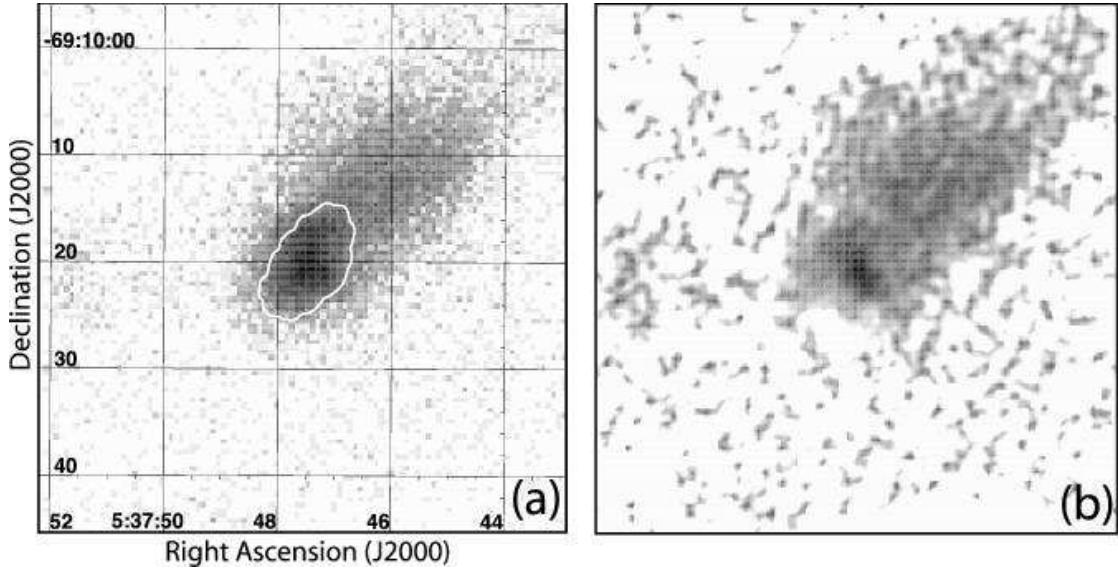


Fig. 10.— The composite SNR N157B, 6.9' off-axis. (a) ACIS data, full-band, binned into  $0.^{\prime\prime}5$  pixels. The 90% contour of the 1.5 keV PSF at the location of the pulsar is shown in white. (b) Maximum likelihood reconstruction of (a), 64 iterations.

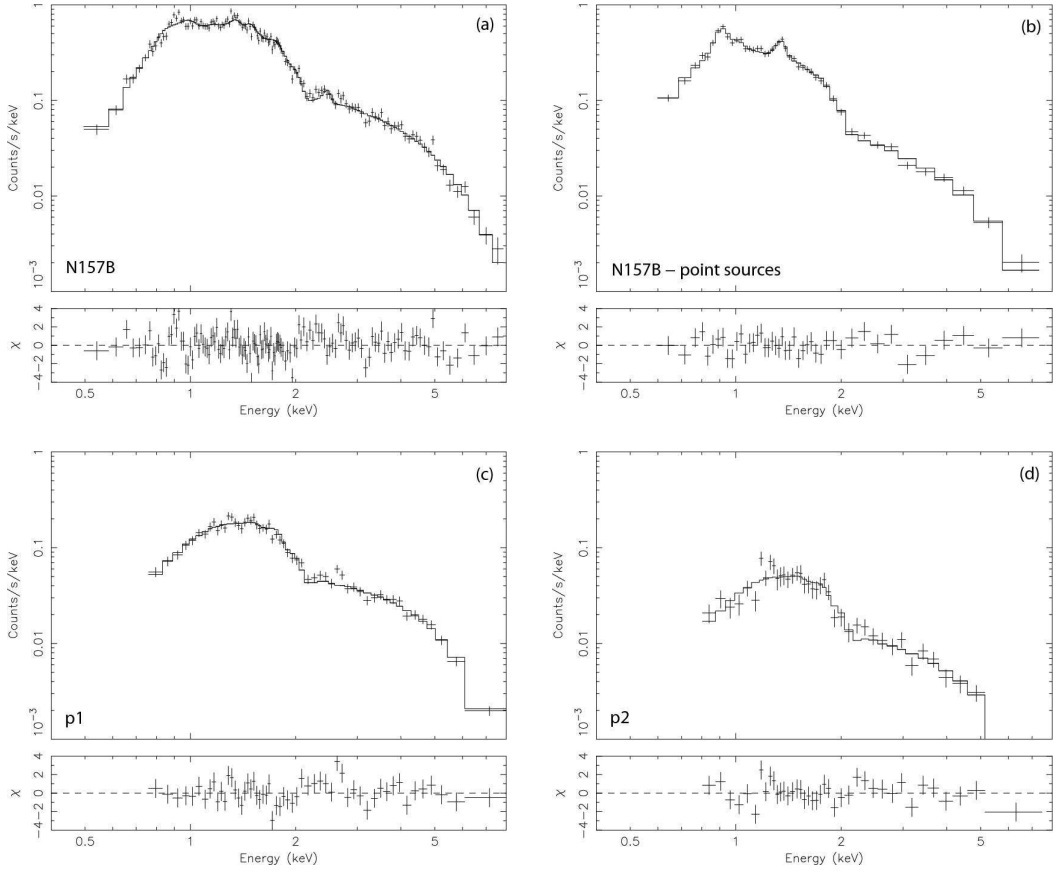


Fig. 11.— Spectra of the X-ray emission in N157B. (a) The composite spectrum of the entire N157B SNR (as outlined in Figure 2), including all point sources. (b) Diffuse emission in the same region (excluding all point sources). (c) The slightly piled-up spectrum of the pulsar (region p1). (d) Region p2, the pointlike structure in the N157B cometary nebula.

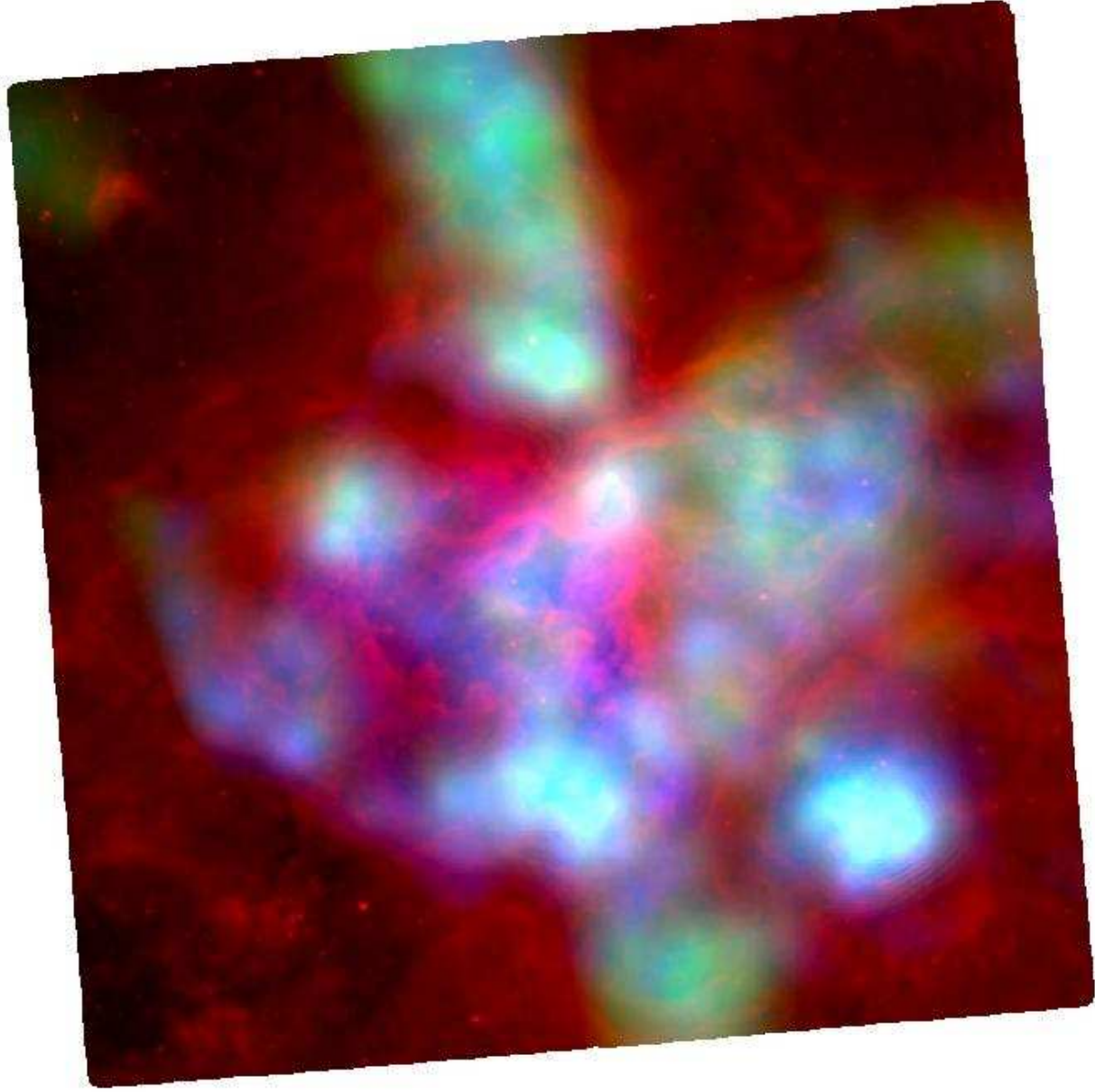


Fig. 12.—X-ray diffuse structures in the HII region context: red = MCELS H $\alpha$ , green = ACIS 350–900 eV, blue = ACIS 900–2300 eV.

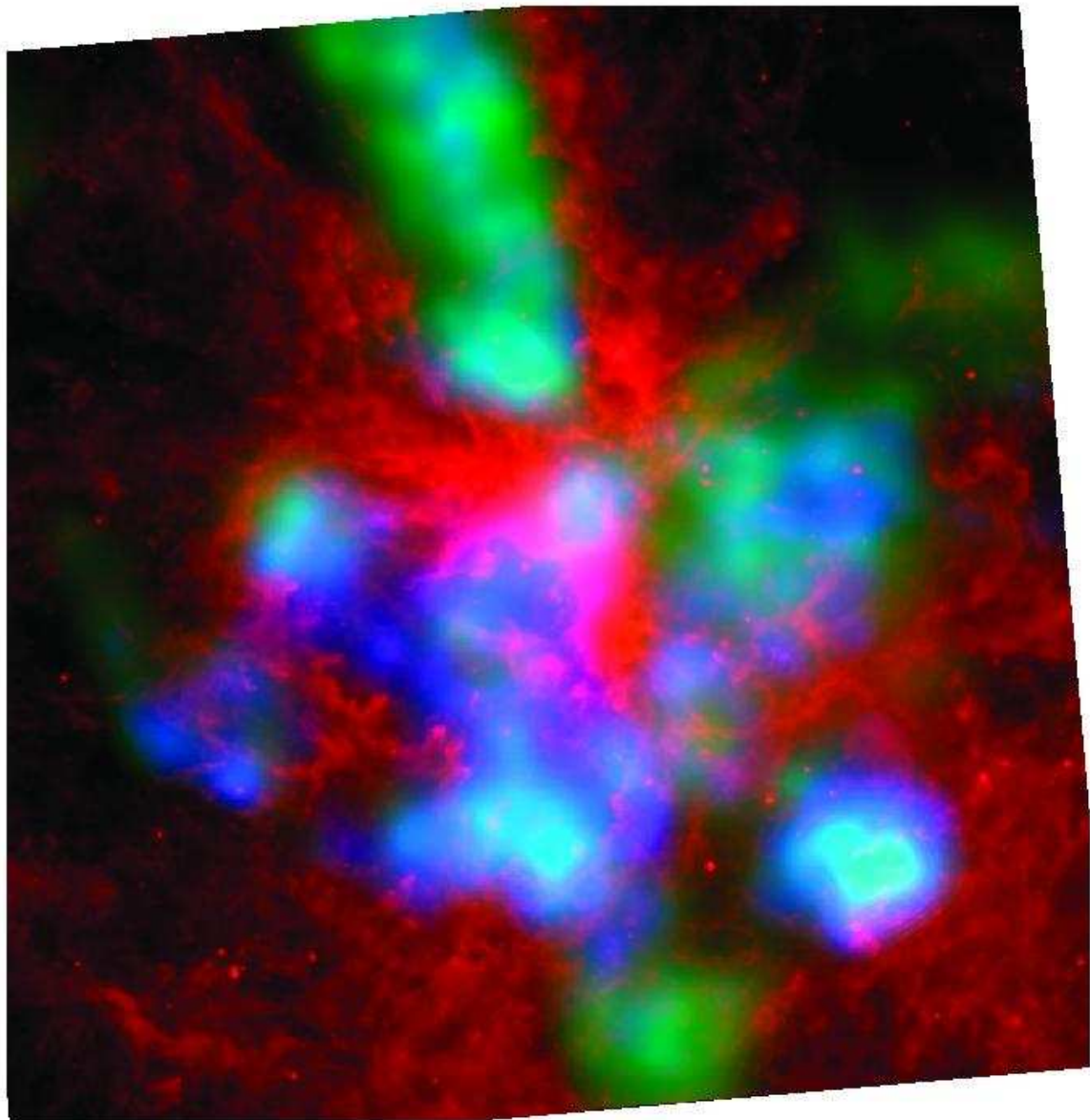


Fig. 13.— A composite of the new mid-infrared ( $6.5\text{--}9.4\mu\text{m}$ ) *Spitzer*/IRAC image of 30 Dor (in red) with the 350–900 eV and 900–2300 eV adaptively smoothed *Chandra*/ACIS images (in green and blue). This *Spitzer* image was the subject of a January 2004 NASA press release (BRB, PI).

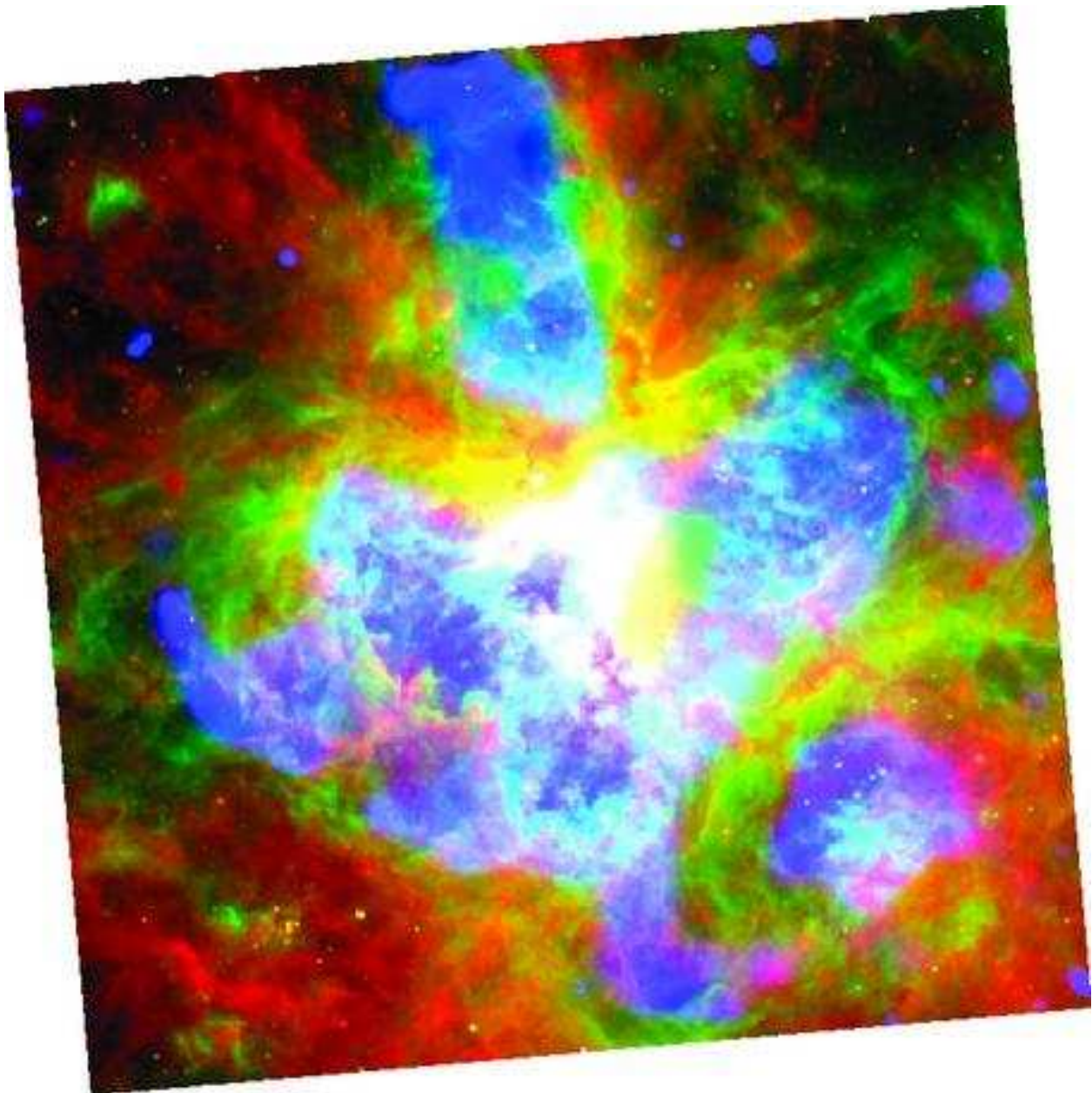


Fig. 14.— X-ray diffuse structures in the broader context: red = *Spitzer*/IRAC 6.5–9.4 $\mu$ m, green = MCELS H $\alpha$ , blue = *Chandra*/ACIS 900–2300 eV. X-ray emission is scaled to show large-scale structures.

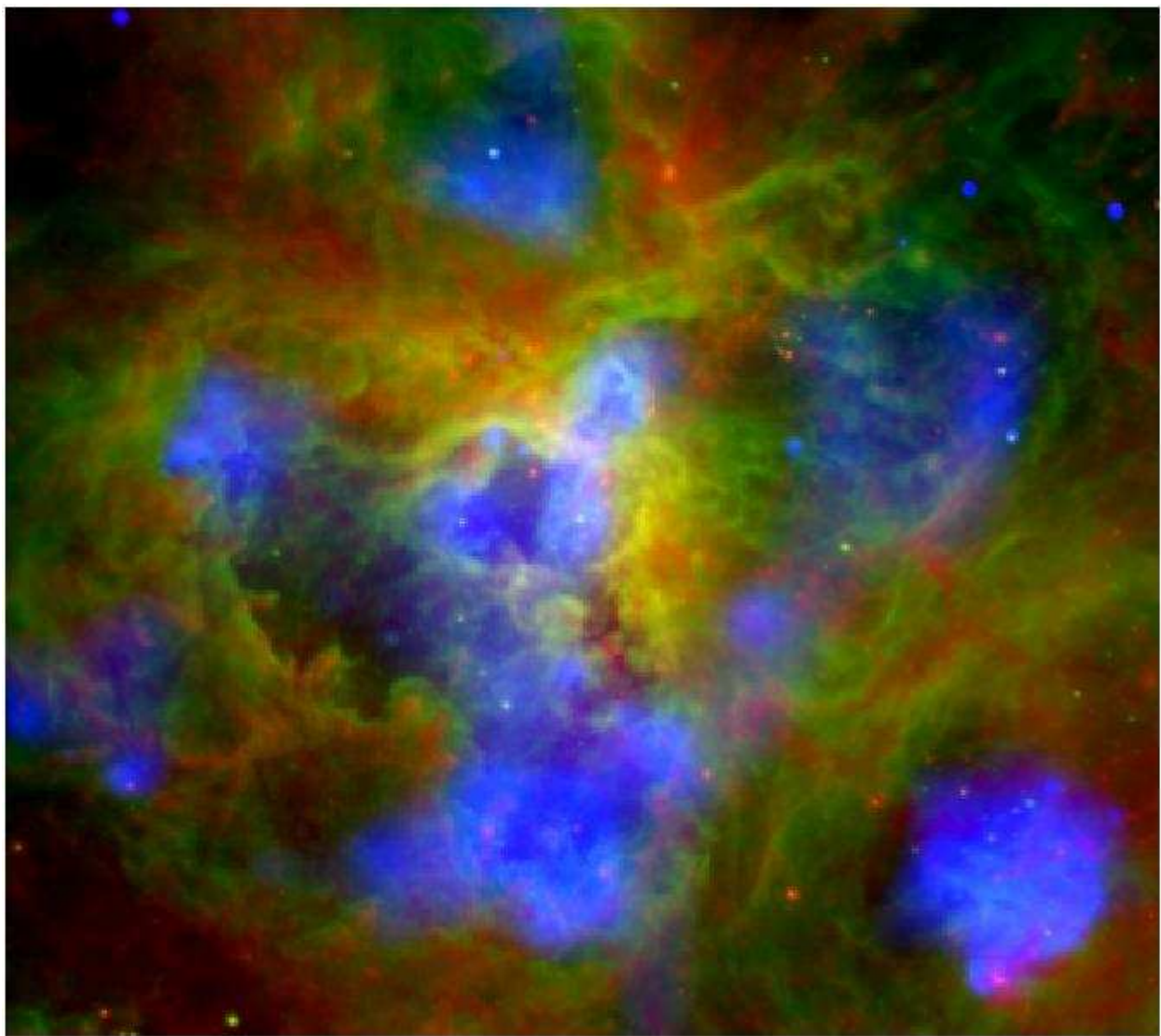


Fig. 15.— The central  $13'.9 \times 12'.5$  of Figure 14, centered on R136 and scaled to show just the brighter diffuse X-ray structures.

TABLE 1  
LOG OF *Chandra* OBSERVATIONS

| Obs ID      | Start Time (UT)<br>1999 Sep 21 | Exposure<br>Time (s) | Frame<br>Time (s) | Active<br>CCDs | Mode <sup>a</sup> |
|-------------|--------------------------------|----------------------|-------------------|----------------|-------------------|
| 22          | 19:48                          | 1049                 | 3.2               | 012367         | F                 |
| 62520 long  | 20:40                          | 20613                | 3.3               | 012378         | VF                |
| 62520 short | 20:40                          | 208                  | 0.3               | 012378         | VF                |

<sup>a</sup>The observing mode: F=Faint, VF=Very Faint.

NOTE.—Exposure times are the net usable times after various filtering steps are applied in the data reduction process. Nominal pointing (in decimal degrees) for all observations was RA (J2000) = 84.68730356, Dec (J2000) = -69.0954973, with a roll angle of 85°. These quantities are obtained from the satellite aspect solution before astrometric correction is applied.

TABLE 2  
X-RAY SPECTROSCOPY OF 30 DOR GLOBAL EMISSION

| Emission Component | Net Counts | Spectral Fit Parameters <sup>a</sup> |               |                            |          |                   |                     | Abundances > $0.3Z_{\odot}$ |      |      |      | X-ray Luminosities <sup>b</sup> |            |                                     |            |                |
|--------------------|------------|--------------------------------------|---------------|----------------------------|----------|-------------------|---------------------|-----------------------------|------|------|------|---------------------------------|------------|-------------------------------------|------------|----------------|
|                    |            | $\log N_H$<br>(cm $^{-2}$ )          | $kT$<br>(keV) | $\log EM$<br>(cm $^{-3}$ ) | $\Gamma$ | $\log N_{\Gamma}$ | $\chi^2/\text{dof}$ | O                           | Ne   | Mg   | S    | $\log L_s$                      | $\log L_h$ | $\log L_{p,c}$<br>(ergs s $^{-1}$ ) | $\log L_t$ | $\log L_{t,c}$ |
| (1)                | (2)        | (3)                                  | (4)           | (5)                        | (6)      | (7)               | (8)                 | (9)                         | (10) | (11) | (12) | (13)                            | (14)       | (15)                                | (16)       | (17)           |
| all                | 55767      | 21.6                                 | 0.35          | 60.03                      | 2.3      | -2.3              | 256/157             | 0.6                         | 0.8  | 0.6  | ...  | 36.51                           | 36.29      | 36.31                               | 36.71      | 37.15          |
| all - N157B        | 35634      | 21.6                                 | 0.37          | 59.93                      | 2.8      | -2.8              | 149/95              | 0.6                         | 0.8  | 0.6  | 1.5  | 36.35                           | 35.61      | 35.64                               | 36.42      | 36.95          |
| diffuse            | 32306      | 21.4                                 | 0.58          | 59.58                      | ...      | ...               | 146/85              | 1.2                         | 1.1  | 0.7  | ...  | 36.32                           | 35.09      | 35.12                               | 36.34      | 36.67          |
| pt srcs            | 2954       | 21.5                                 | 1.0           | 58.19                      | 1.8      | -3.3              | 106/103             | ...                         | ...  | ...  | ...  | 35.31                           | 35.63      | 35.65                               | 35.80      | 35.95          |
| N157B              | 20216      | 21.6                                 | 0.71          | 58.88                      | 2.1      | -2.6              | 243/130             | 0.8                         | ...  | 1.1  | 2.1  | 35.98                           | 36.17      | 36.20                               | 36.39      | 36.62          |

<sup>a</sup>All thermal plasma fits were  $wabs*(apec + powerlaw)$  or  $wabs*(vapec + powerlaw)$  in XSPEC and assumed abundances of  $0.3Z_{\odot}$  for all elements unless otherwise noted.  $\Gamma$  is the power law photon index,  $N_{\Gamma}$  is the power law normalization (in units of photons cm $^{-2}$  s $^{-1}$  keV $^{-1}$  at 1 keV), “dof” = degrees of freedom, and  $\chi^2/\text{dof}$  represents the goodness of fit.

<sup>b</sup>X-ray luminosities: s = soft band (0.5–2 keV); h = hard band (2–8 keV); t = total band (0.5–8 keV). Absorption-corrected luminosities are subscripted with a c.

NOTE.—See §4.3 for descriptions of the columns. Uncertainties (90% confidence intervals) on  $\log N_H$  are  $\leq \pm 0.07$ . Uncertainties on  $kT$  are  $\leq \pm 0.04$  except for the composite point source fit, where  $kT = 1.0^{+0.23}_{-0.14}$ . Uncertainties on the power law slope  $\Gamma$  are  $\leq \pm 0.3$ . Uncertainties on  $\log EM$ ,  $\log N_{\Gamma}$ , and abundances are typically  $\pm 0.1$  or smaller except for the sulfur abundance, which is not as well constrained. A distance of 50.0 kpc was assumed throughout.

TABLE 3  
X-RAY SPECTROSCOPY OF DIFFUSE REGIONS

| Diff<br>Reg | Net<br>Counts | Spectral Fit Parameters <sup>a</sup> |               |                                  |          |            |                     | Abundances > $0.3Z_{\odot}$ |      |            |        | X-ray Luminosities <sup>b</sup> |            |   |            | Diffuse<br>Area<br>(arcmin <sup>2</sup> ) | $\log S_{X^{-1}}$<br>(ergs s <sup>-1</sup><br>pc <sup>-2</sup> ) |
|-------------|---------------|--------------------------------------|---------------|----------------------------------|----------|------------|---------------------|-----------------------------|------|------------|--------|---------------------------------|------------|---|------------|---|--|
|             |               | $\log N_H$<br>(cm <sup>-2</sup> )    | $kT$<br>(keV) | $\log EM$<br>(cm <sup>-3</sup> ) | $\Gamma$ | $\log N_F$ | $\chi^2/\text{dof}$ | O                           | Ne   | Mg         | Other  | hi                              | $\log L_s$ | $\log L_{s,c}$<br>(ergs s <sup>-1</sup> ) | $\log L_t$ | $\log L_{t,c}$                            |  |
| #<br>(1)    | (2)           | (3)                                  | (4)           | (5)                              | (6)      | (7)        | (8)                 | (9)                         | (10) | (11)       | (12)   | (13)                            | (14)       | (15)                                      | (16)       | (17)                                      | (18)   |
| 1           | 37299         | 21.6                                 | 0.3           | 60.0                             | 2.8      | -2.6       | 163/102             | 0.6                         | 0.8  | 0.6        | ...    | 36.4                            | 37.0       | 36.4                                      | 37.0       | 101.37                                    | 32.7   |
| 2           | 4039          | 21.4                                 | 0.6           | 58.7                             | ...      | ...        | 59/51               | 1.2                         | 0.5  | 0.6        | ...    | 35.4                            | 35.8       | 35.4                                      | 35.8       | 56.38                                     | 31.7   |
| 3           | 1355          | 21.6                                 | 0.3           | 58.8                             | ...      | ...        | 60/40               | 0.5                         | 0.7  | 0.7        | ...    | 35.0                            | 35.7       | 35.0                                      | 35.7       | 6.91                                      | 32.5   |
| 4           | 360           | 21.3                                 | 0.3           | 58.0                             | ...      | ...        | 11/13               | 0.5                         | 0.9  | 1.2        | ...    | 34.4                            | 34.8       | 34.4                                      | 34.9       | 1.00                                      | 32.5   |
| 5           | 840           | 21.7                                 | 0.3           | 58.8                             | ...      | ...        | 28/31               | ...                         | ...  | ...        | ...    | 34.7                            | 35.5       | 34.7                                      | 35.5       | 1.40                                      | 33.1   |
| 6           | 355           | 21.7                                 | 0.4           | 57.9                             | ...      | ...        | 24/25               | hi                          | hi   | hi         | Al     | 34.3                            | 34.9       | 34.3                                      | 34.9       | 0.63                                      | 32.8   |
| 7           | 608           | 21.8                                 | 0.4           | 58.3                             | ...      | ...        | 39/41               | 1.8                         | 1.4  | ...        | ...    | 34.5                            | 35.5       | 34.6                                      | 35.5       | 1.06                                      | 33.1   |
| 8           | 458           | 21.7                                 | 0.4           | 58.1                             | ...      | ...        | 29/36               | 1.2                         | 1.3  | 0.8        | ...    | 34.4                            | 35.2       | 34.4                                      | 35.2       | 1.07                                      | 32.9   |
| 9           | 1460          | 21.7                                 | 0.6           | 58.5                             | ...      | ...        | 44/39               | 1.3                         | ...  | ...        | ...    | 34.9                            | 35.5       | 35.0                                      | 35.6       | 4.49                                      | 32.6   |
| 10          | 3454          | 21.8                                 | 0.4           | 59.3                             | ...      | ...        | 56/43               | 0.5                         | 0.7  | 0.6        | ...    | 35.3                            | 36.2       | 35.3                                      | 36.2       | 8.93                                      | 32.9   |
| 11          | 2338          | 21.7                                 | 0.4           | 58.8                             | ...      | ...        | 44/34               | 1.0                         | 1.3  | 0.9        | ...    | 35.2                            | 35.8       | 35.2                                      | 35.8       | 2.54                                      | 33.1   |
| 12          | 2194          | 21.8                                 | 0.5           | 58.9                             | ...      | ...        | 35/36               | ...                         | 0.9  | 0.7        | ...    | 35.1                            | 35.8       | 35.2                                      | 35.8       | 12.49                                     | 32.4   |
| 13          | 1223          | 21.8                                 | 0.3           | 59.1                             | ...      | ...        | 20/34               | ...                         | ...  | ...        | ...    | 34.9                            | 35.8       | 34.9                                      | 35.8       | 3.65                                      | 32.9   |
| 14          | 854           | 21.5                                 | 0.6           | 58.2                             | ...      | ...        | 34/40               | ...                         | ...  | ...        | ...    | 34.7                            | 35.2       | 34.8                                      | 35.2       | 3.26                                      | 32.3   |
| 15          | 222           | 21.8                                 | 0.8           | 57.8                             | ...      | ...        | 26/32               | ...                         | ...  | ...        | ...    | 34.1                            | 34.7       | 34.2                                      | 34.8       | 2.73                                      | 32.0   |
| 16          | 2598          | 21.4                                 | 0.5           | 58.7                             | ...      | ...        | 70/38               | 0.7                         | 0.8  | 0.5        | ...    | 35.2                            | 35.6       | 35.2                                      | 35.6       | 12.48                                     | 32.2   |
| 17          | 2939          | 21.4                                 | 0.5           | 57.6                             | ...      | ...        | 28/21               | 1.1                         | 1.1  | ...        | ...    | 35.3                            | 35.7       | 35.3                                      | 35.7       | 7.97                                      | 32.4   |
| 18          | 1092          | 21.7                                 | 0.3           | 58.7                             | ...      | ...        | 41/23               | 1.3                         | 1.1  | ...        | ...    | 34.9                            | 35.8       | 34.9                                      | 35.8       | 10.00                                     | 32.5   |
| 19          | 122           | 21.6                                 | 0.3           | 57.8                             | ...      | ...        | 19/13               | ...                         | ...  | ...        | ...    | 33.9                            | 34.6       | 33.9                                      | 34.6       | 2.42                                      | 31.8   |
| 20          | 309           | 21.6                                 | 0.6           | 57.8                             | ...      | ...        | 36/35               | ...                         | ...  | ...        | ...    | 34.2                            | 34.7       | 34.2                                      | 34.7       | 2.07                                      | 32.1   |
| 21          | 86            | 21.5                                 | 0.6           | 57.2                             | ...      | ...        | 11/13               | ...                         | ...  | ...        | ...    | 33.7                            | 34.2       | 33.7                                      | 34.2       | 1.16                                      | 31.8   |
| 22          | 158           | 21.7                                 | 0.3           | 57.8                             | ...      | ...        | 20/18               | ...                         | hi   | hi         | Al     | 34.0                            | 34.7       | 34.0                                      | 34.7       | 3.62                                      | 31.8   |
| 23          | 228           | 21.1                                 | 0.3           | 57.8                             | ...      | ...        | 30/35               | ...                         | ...  | ...        | ...    | 34.3                            | 34.5       | 34.3                                      | 34.5       | 4.59                                      | 31.5   |
| 24          | 2692          | 21.2                                 | 0.5           | 58.4                             | ...      | ...        | 59/39               | 1.1                         | 0.8  | 0.6        | ...    | 35.2                            | 35.5       | 35.3                                      | 35.5       | 12.70                                     | 32.1   |
| 25          | 1050          | 21.5                                 | 0.3           | 58.6                             | ...      | ...        | 41/37               | 0.6                         | ...  | ...        | Si=0.8 | 34.8                            | 35.5       | 34.9                                      | 35.5       | 1.95                                      | 32.8   |
| 26          | 493           | 21.6                                 | 0.3           | 58.5                             | ...      | ...        | 21/20               | ...                         | ...  | ...        | ...    | 34.5                            | 35.2       | 34.5                                      | 35.2       | 1.54                                      | 32.7   |
| 27          | 880           | 21.2                                 | 0.5           | 58.0                             | ...      | ...        | 29/35               | 1.3                         | 0.9  | ...        | ...    | 34.8                            | 35.0       | 34.8                                      | 35.1       | 2.38                                      | 32.3   |
| p1          | 6129          | 21.8                                 | ...           | 2.0                              | -2.9     | 67/56      | ...                 | ...                         | ...  | ...        | 35.4   | 35.9                            | 36.1       | 36.2                                      | 0.02       | 35.3                                      |  |
| p2          | 1515          | 21.8                                 | ...           | 2.3                              | -3.3     | 38/36      | ...                 | ...                         | ...  | ...        | 34.9   | 35.5                            | 35.4       | 35.7                                      | 0.02       | 34.8                                      |  |
| n0          | 1754          | 21.8                                 | ...           | 2.5                              | -3.3     | 28/47      | ...                 | ...                         | ...  | ...        | 34.9   | 35.5                            | 35.4       | 35.7                                      | 0.05       | 34.5                                      |  |
| n1          | 1869          | 21.8                                 | 0.6           | 57.2                             | 2.4      | -3.4       | 45/42               | hi                          | hi   | Al, Si, Ar | 34.9   | 35.5                            | 35.4       | 35.7                                      | 0.09       | 34.2                                      |  |
| n2          | 849           | 21.7                                 | 0.9           | 57.5                             | 2.7      | -3.8       | 33/29               | ...                         | ...  | S, Ca      | 34.6   | 35.2                            | 35.0       | 35.3                                      | 0.11       | 33.8                                      |  |
| n3          | 649           | 21.5                                 | 0.7           | 57.7                             | 2.6      | -4.2       | 34/23               | ...                         | ...  | Al         | 34.6   | 35.0                            | 34.7       | 35.0                                      | 0.19       | 33.4                                      |  |
| n4          | 1130          | 21.6                                 | 0.3           | 56.3                             | 3.4      | -3.7       | 33/37               | hi                          | hi   | Al, Si, S  | 34.8   | 35.4                            | 34.9       | 35.4                                      | 0.45       | 33.4                                      |  |
| n5          | 1264          | 21.7                                 | 0.3           | 58.5                             | 3.5      | -3.7       | 47/27               | 0.7                         | hi   | hi         | ...    | 34.9                            | 35.7       | 35.0                                      | 35.7       | 1.01                                      | 33.4   |
| n6          | 1032          | 21.8                                 | 0.3           | 58.8                             | 2.2      | -4.3       | 30/26               | 0.7                         | 0.8  | 0.6        | ...    | 34.8                            | 35.7       | 34.9                                      | 35.7       | 1.89                                      | 33.1   |
| n7          | 1022          | 21.5                                 | 0.7           | 58.2                             | ...      | ...        | 54/31               | 1.4                         | ...  | 0.6        | ...    | 34.8                            | 35.2       | 34.8                                      | 35.2       | 5.03                                      | 32.2   |
| n8          | 9755          | 21.5                                 | 0.3           | 58.4                             | 2.6      | -2.8       | 36/38               | ...                         | hi   | hi         | ...    | 35.7                            | 36.1       | 36.0                                      | 36.3       | 9.78                                      | 32.8   |

<sup>a</sup>All thermal plasma fits for regions 1–27 were *wabs\*(appec)* or *wabs\*(vapecc)* in XSPEC and assumed  $0.3Z_{\odot}$  abundances for all elements unless otherwise noted. Fits to region 1 and N157B (p1–n8) additionally included a power law component.  $\Gamma$  is the power law photon index,  $N_F$  is the power law normalization, “dof” = degrees of freedom, and  $\chi^2/\text{dof}$  represents the goodness of fit.

<sup>b</sup>X-ray luminosities: s = soft band (0.5–2 keV); h = hard band (2–8 keV); t = total band (0.5–8 keV). Absorption-corrected luminosities are subscripted with a c.

<sup>c</sup>Soft band surface brightness, corrected for absorption.

NOTE.—See §5.2 for descriptions of the columns. Quantities in *italics* were frozen in the spectral fit; see the text for details. A distance of 50.0 kpc was assumed throughout; at that distance,  $1'^2 \simeq 211 \text{ pc}^2$ . Uncertainties are omitted due to space constraints in the table; they depend on the number of counts used in the fit of course but are typically similar to the uncertainties described in the Table 2 notes.

TABLE 4  
ACIS SPECTRAL EXTRACTION REGIONS AND H $\alpha$  KINEMATICS

| ACIS Region       | CK94 Echellogram | CK94 Notes                               | Expansion velocity (km s $^{-1}$ ) |
|-------------------|------------------|--|------------------------------------|
| 5                 | Fig. 7b          | R139W fast shell                         | -120                               |
| 6                 | Fig. 7a          | R136E fast shell                         | -130                               |
| 5 left edge, 9    | Fig. 6d          | R136's massive slow shell                | $\pm 40$                           |
| 7, 10, 11         | Fig. 3           | Shell 1 network                          | 70 and higher                      |
| 8                 | Fig. 7g          | $\sim 1'$ extended high-velocity feature | 90–120                             |
| 11                | Fig. 3           | Shell 1 south rim                        | 70 and higher                      |
| 13 left of center | Fig. 6b          | 2.4' slow shell                          | 85                                 |
| 13 right half     | Fig. 7h          | 30'' high-velocity feature               | > -100                             |
| 15 left half      | ...              | 20 pc fast shell between Shells 1 & 2    | 110                                |
| 16–19             | Fig. 8           | Shell 3 network                          | 20–200                             |
| 17 (West Ring)    | Fig. 7c & d      | NW Loop fast shell                       | -200                               |
| 24, 26, 27        | Fig. 7f          | Shell 5 network                          | 60 and higher                      |
| 25 top            | Fig. 6c          | slow shell                               | 70                                 |

NOTE.—CK94 = Chu & Kennicutt (1994); echellogram labels refer to figure numbers from that paper.